Neural dynamics for working memory and evidence integration during olfactory navigation in *Drosophila*

Nicholas D. Kathman, Aaron J. Lanz, Jacob D. Freed, Katherine I. Nagel*

Department of Neuroscience, NYU School of Medicine
*Lead contact: katherine.nagel@nyumc.org

Abstract

To navigate towards an unknown food source, animals must accumulate evidence about the location of a goal and store this information in working memory. Here we identify a population of local neurons in the fan-shaped body of *Drosophila* that exhibits both evidence integration and working memory dynamics. Imaging from these neurons during virtual odor-guided navigation reveals a bump of activity that is activated by odor, but can outlast the odor stimulus by several seconds. Persistent bump activity is associated with persistent movement in the direction adopted during odor, arguing that these neurons represent a directional working memory. When the fly navigates a virtual odor plume, bump activity slowly ramps up with successive odor encounters, indicating that it integrates odor information over time. We do not observe these dynamics in a set of neighboring local neurons, although both populations show slow modulation correlated with engagement in the task. Silencing the first population impairs the integration of odor encounters and the persistence of upwind heading. Our work identifies a small group of genetically-identified neurons that integrate and store stochastic sensory evidence to support navigation in complex natural environments.

Introduction

In many real-world navigation tasks, sensory information about the direction and location of a goal is only intermittently available. For example, an owl hunting a mouse by sound might get only sporadic and uncertain information about the location of its prey, or a leopard chasing an antelope by sight might have its view interrupted by brush. In such tasks, the ability to accumulate sensory information about the direction of a target over time, and to hold that information in working memory during loss of sensory input are critical to success. While the neural mechanisms underlying the processes of evidence integration and working memory have been the subject of extensive investigations (Brody and Hanks, 2016; Wang, 2021), it is still not clear where such information is accumulated and stored to guide natural behaviors (Khona and Fiete, 2022; Gupta et al., 2024).

Many animals use odor cues to navigate towards the unknown location of a food source (Gray et al., 2005; Álvarez-Salvado et al., 2018; Baker et al., 2018; Demir et al., 2020). Because odor plumes are turbulent, they generate stochastic cues that must be integrated and stored in memory in order to navigate effectively (David et al., 1983; Dekker and Cardé, 2011; Riffell et al., 2014; van Breugel and Dickinson, 2014). Behavioral studies in plumes argue that insects integrate odor encounters over time to drive navigational decisions (Demir et al., 2020), while theoretical studies suggest that a simple form of working memory that allows an insect to continue its trajectory in the absence of odor can promote more effective source finding (Verano et al., 2023). However, the potential neural substrate of these computations is unknown.

Recent evidence suggests that the fan-shaped body (FB), a part of the insect navigation center called the Central Complex (CX), is a key location for computing a goal direction during navigation. Output neurons of the FB can compare the fly's current heading to a goal signal expressed in allocentric (world-centered) coordinates to steer the fly in a target direction (Stone et al., 2017; Mussells-Pires et al., 2024; Westeinde et al., 2024). Patterned activation of certain FB local neurons can drive goal-directed walking relative to a visual landmark (Mussells-Pires et al., 2024), or to the wind (Matheson et al., 2022), consistent with the idea that FB local neurons can encode allocentric goals. The FB is ideally positioned to play a role in odor-guided navigation. It receives odor information through a set of wide-field tangential neurons that are downstream of the associative learning center in the mushroom body (Li et al., 2020; Scaplen et al., 2021; Matheson et al., 2022). Activation of some of these tangential inputs, and also of some FB local neurons, can drive orientation upwind (Matheson et al., 2022; Aso et al., 2023), while broad developmental disruption of the CX completely abolishes odor-gated wind orientation behavior (Hamid et al., 2024). However, the *in vivo* dynamics of FB goal signals and their precise role in natural navigation tasks are not known.

In a recent study, we identified FB local neurons labeled by the line VT062617-Gal4 whose sparse activation can drive movement in a goal direction relative to the wind (Matheson et al., 2022). Here we developed a closed-loop virtual paradigm to examine the activity of these neurons during odor-guided navigation. We find that these neurons exhibit a bump of activity that is activated by odor but persists after odor offset for variable intervals. While the bump remains active, we find that flies continue running in the direction adopted during odor, arguing that these neurons represent a short-term directional goal memory. By simulating a turbulent plume in closed-loop, we show that these neurons integrate olfactory evidence over a period of several seconds, a property not shared by a second group of local neurons. Finally, we use optogenetic silencing to show that the activity of these neurons is necessary for the gain of olfactory evidence accumulation, and for persistent directional running after odor loss. Our findings reveal internal dynamics that shape the transformation of stochastic sensory input into goal-directed navigation behavior.

Results

Olfactory working memory activity in a set of FB local neurons

To investigate the activity of VT062617 neurons during olfactory navigation, we developed a paradigm in which a tethered fly walking on an air-supported ball can navigate a virtual odor and wind environment (Fig. 1A; see Methods). We monitored ball movements to compute the fly's orientation, which then can drive changes in wind direction relative to the fly. In a first set of experiments, we rotated the wind in closed-loop with the fly's movement, and presented single pulses of the attractive odor apple cider vinegar (5% dilution in water). Similar to previous studies in both freely-walking (Álvarez-Salvado et al., 2018; Demir et al., 2020) and tethered flies (Handler et al., 2019; Zolin et al., 2021), we observed that flies walked more strongly upwind during odor compared to the pre-wind baseline period (Fig. 1B, C). In some trials, flies showed looping behavior after odor offset (Fig. 1B), similar to search behavior evoked by odor loss in freely walking flies (Álvarez-Salvado et al., 2018; Handler et al., 2019; Gattuso et al., 2024).

We imaged from VT062617 neurons (Supp. Fig. 1A) as flies walked in a closed-loop wind environment with odor pulses of 15s duration every ~80-90 seconds (Supp. Fig. 1B). Processes of these neurons in the dorsal fan-shaped body showed a bump of activity that was limited to a few columns (Fig. 1D,E) and was most strongly activated by odor (Fig. 1F,G). The bump was weakly or transiently activated by wind alone in some trials (Fig. 1F) but was largely absent in interleaved trials without airflow (Supp. Fig. 1C,D). Notably, odor-evoked activity could persist after odor offset, with the precise timing varying across trials and flies, and the median offset time ranging from -0.32 to 9.33 s after odor OFF (Fig. 1F-H). Across flies, the median bump offset peaked at ~4 seconds after nominal odor offset (Supp. Fig. 1E). Measurements using a photoionization detector showed a very small residual odor signal following odor offset (Supp. Fig. 1B) with no abrupt change around the time of bump offset. We conclude that the bump reflects persistent neural activity rather than ongoing olfactory input.

We next asked whether persistent activity in VT062617 neurons correlates with aspects of navigation behavior. In several example trajectories (Fig. 1D), we observed that persistent activity was associated with continued straight movement in the direction adopted during odor. To test whether this observation held across trials and flies, we first computed a straightness index (see Methods), and examined the mean straightness for each fly in the presence and absence of a bump. During the odor period, we found that flies tended to walk straight regardless of whether a bump was present. However, during the post-odor period, the presence of a bump was associated with greater straightness (Fig. 1I). Next, we detected offsets for all bumps of at least 5 s duration, and plotted features of trajectories associated with these events (Fig. 1J). We found that bump offset was followed by an increase in angular speed, and a slow deviation of the fly's heading from the "goal" heading adopted during odor (Fig. 1J,K). Since flies mostly travel upwind during odor, heading also deviated from upwind following bump offset (Supp. Fig. 1F) although not as strongly as from the "goal" direction. Finally, we projected the fly's heading onto the goal direction (θ_{goal}, Supp. Fig. 1G) during the post-odor period and found

that this decreased significantly between bump ON and bump OFF periods (Fig. 1L). These data argue that persistent activity in VT062617 neurons represents a directional working memory that allows the fly to continue its trajectory after the loss of odor input.

Bump position does not track heading but can slowly remap during persistent turning

Compass neurons in the fly ellipsoid body exhibit a bump of activity that tracks the fly's heading during virtual navigation (Seelig and Jayaraman, 2015), while FC2 local neurons of the FB exhibit a bump that remains stationary during heading shifts, arguing that its location represents a fixed allocentric goal (Mussells-Pires et al., 2024). To determine the nature of the bump position signal in VT062617 neurons, we examined the relationship between heading and bump position. We observed that the VT062617 bump typically did not shift, even when the fly changed heading (Fig. 2A, top examples) although it could occasionally shift with slow changes in heading (Fig. 2A, bottom example). Across trials and flies we detected low correlations between heading and bump position (Fig. 2B). A limitation of this analysis is that the VT062617 bump is mostly present during odor, when the fly tends to adopt a straight trajectory. Thus, the lack of correlation between heading and bump position might reflect the fact that few headings are explored during periods when the bump is active.

To examine the relationship between heading and bump position more closely, we performed a set of wind-shift experiments, in which we shifted the wind direction by 90° in the middle of the odor period (Fig. 2C-F). In these experiments, we found that while shifting the wind direction could produce a shift in heading (Fig. 2D), we observed only small and non-significant shifts in bump position on these trials (Fig. 2E,F). As a further test of whether VT062617 neurons encode a heading signal, we performed open-loop probe trials—interleaved with previously described closed-loop trials— in which the wind position was fixed at either from 45° left or 45° right of the fly (Fig. 2G,H). This configuration drove flies to turn repeatedly towards the wind for the duration of the odor stimulus (Fig. 2I), however bump position did not rotate concurrently, as would be expected of a compass signal (Fig. 2G,H). We did observe that in many of these trials the bump slowly shifted across the FB in the direction opposite to turning— from left to right columns when wind was presented on the left and from right to left columns when wind was presented on the right (Fig. 2G,H,J). Left- and right- positioned wind produced opposing and significantly different shifts in bump position (Fig. 2J). However, the gain of bump movement was typically very low, with multiple rotations of the fly required to shift the bump by a few columns (Fig. 2K). We observed similar low-gain position shifts in some closed-loop trials (Fig. 2A, Supp. Fig. 2C) arguing that they are driven by fly movement, rather than by the stimulus configuration. These data indicate that the fly can update the position of the bump, but with a low and variable gain relative to its behavior. We conclude that bump position in VT062617 neurons does not represent heading, but more likely represents an internal estimate of a goal direction (see Discussion).

Olfactory evidence accumulation during turbulent plume navigation

We next sought to examine the activity of VT062617 neurons during a more complex navigation task. In natural environments, odors form turbulent plumes in which odor fluctuates stochastically as a function of distance and direction to the source (Boie et al., 2018; Ackels et al., 2021). To implement a virtual plume environment, we leveraged a previously recorded movie of odor concentrations in a boundary layer plume at approximately fly height and windspeed comparable to our experiment (Connor et al., 2018, Methods, Fig. 3A). As the fly navigated in 2D, we used time and the virtual position of the fly to index into this movie and determine the odor concentration at the virtual location of the fly. We then used an adaptive compression algorithm (Álvarez-Salvado et al., 2018) that mimics aspects of peripheral olfactory encoding (Victor et al., 2019) to binarize this concentration relative to an adaptive threshold, and delivered the resulting odor pulses to the fly using temporally precise odor valves (Supp. Fig. 3A). As a result of this algorithm, a fly navigating our virtual odor plume encounters a stochastic series of odor pulses that increase in frequency as it approaches the fictive source.

Plume navigation revealed additional dynamics in VT062617 neurons. As the fly navigated the plume, we observed initially weak responses to odor that grew gradually with repeated odor encounters (Fig. 3B). We also observed instances where a series of odor encounters ignited a long-lasting bump of activity, that was again associated with maintaining a straight trajectory (Fig. 3C). To quantify bump dynamics in this more variable sensory environment, we computed instantaneous odor encounter frequency and plotted bump activity as a function of odor encounter frequency at different intervals after the last odor offset (Demir et al., 2020, Fig. 3D, Supp. Fig. 3B). We observed that bump amplitude grew with odor encounter frequency, and remained high for many seconds after odor offset, consistent with integration of olfactory evidence.

To determine the relationship between bump activity, odor dynamics, and behavior, we computed linear filters between these variables. As odor and locomotion show correlations during navigation, we decorrelated these filters by inverting the correlation matrix between these variables across temporal frequencies (Nagel and Doupe, 2008, see Methods). The filter describing the relationship between odor and neural activity (Fig. 3E, Supp. Fig. 4A) had an “integrating” shape with a single peak that extends ~10 seconds into the past, supporting the idea that these neurons integrate odor information over several seconds. In contrast, the filter relating angular speed (turning) to activity was entirely negative (Fig. 3F, Supp. Fig. 4B), consistent with the observation that activity is strongest during straight walking. We also observed a positive integrating filter for forward velocity (Fig. 3G, Supp. Fig. 4C), although this filter was narrower than the filter for odor. This forward velocity filter supports observations during odor pulse trials, where bump onset was associated with an increase in forward velocity, and forward velocity was higher when a bump was present (Supp. Fig. 4D,E). Our plume experiments thus reveal a temporal integration of odor input, and support our previous finding that persistent activity in VT062617 neurons is associated with faster, straighter, trajectories.

Working memory and evidence integration dynamics are not widespread in the FB

The dynamics we observe in VT062617 neurons might arise within these neurons or might be more broadly shared across this brain area. To address the specificity of these dynamics, we imaged from a second line, 52G12-Gal4, that labels a large set of ventral FB local neurons (Supp. Fig. 5A, B). Imaging from 52G12 neurons in the plume paradigm revealed transient responses to repeated odor encounters without the gradual ramping and persistence we observed in VT062617 neurons (Fig. 4A). The filter relating odor to activity for 52G12 was much narrower than the filter for VT062617, indicating a shorter integration time (Fig. 4B). The filter relating angular speed to activity had a positive peak for 52G12, in contrast to the negative peak for VT062617, indicating a correlation with turning rather than straight walking (Fig. 4C). Consistent with these observations, we found that 52G12 response to single odor pulses were transient rather than persistent (Supp. Fig. 5C,D), and correlated with turning rather than straight walking (Supp. Fig. 5E). Thus, the coding features of VT062617 neurons— gradual integration of olfactory evidence and persistent activity associated with straight trajectories— are not shared across the FB, but are specific to a subset of local neurons.

While neurons labeled by 52G12 and VT062617 showed distinct local encoding dynamics, both showed similar modulation on the slower timescale of trials (Fig. 4D). Many flies walked upwind only on a subset of trials in an experiment. Runs of trials with high upwind displacement could occur both early and late in the experiment for both genotypes, arguing that lack of engagement does not reflect simple sensory habituation. Strikingly, we observed greater activity in both VT062617 and 52G12 neurons during periods when the fly showed strong upwind displacement. Upwind displacement and total bump activity were positively correlated across both genotypes (Fig. 4E), significantly greater than shuffled trials. In VT062617 flies, activity was also significantly correlated with movement probability and forward velocity (Supp. Fig. 5C). These data indicate that while different FB local neurons track distinct local features of odor dynamics and self-motion, activity across the FB is co-regulated on slower timescales.

VT062617 neurons play a causal role in working memory

Our plume experiments argue that VT062617 neurons integrate odor information over time and maintain this information for seconds after odor offset. We therefore wondered if flies show behavioral correlates of these dynamics and if VT062617 neurons play a causal role in navigation. To test the hypothesis that flies integrate odor information across pulses, we presented freely walking flies in a laminar wind tunnel with variable numbers of odor pulses, and examined the dynamics of their orientation behavior (Fig. 5A-C). We found that increasing numbers of odor pulses led to a greater probability of upwind walking, that saturated around 4 pulses (Fig. 5B,C). Upwind walking persisted for 5-10 seconds after the end of the last odor pulse, and decayed with a uniform timecourse across pulse numbers (Fig. 5B).

To ask whether VT062617 neurons play a role in these dynamics, we presented flies expressing the optogenetic silencing agent UAS-GtACR1 in VT062617 neurons with variable numbers of odor pulses. We measured upwind walking in interleaved trials with blue light that silences the neurons, and in the absence of light. We found that silencing VT062617 neurons led to a faster decay in upwind walking across pulse numbers, and a decreased response to the lowest pulse number (Fig. 5D). The probability of walking upwind in the 10s period after odor OFF was significantly reduced for all stimulus configurations (Fig. 5F), while peak upwind walking was reduced for the single pulse condition (Fig. 5G). In genetic control flies, light had no effect on the gain or persistence of upwind walking (Fig. 5E,H,I). We conclude that VT062617 neurons are causally required for both the gain of evidence accumulation and the persistence of upwind walking after odor loss.

Discussion

Working memory and evidence integration in a genetically tractable central brain circuit

Working memory and evidence integration are fundamental building blocks of cognition, whose neural substrates have been studied extensively in non-human primates (Funahashi et al., 1989; Wimmer et al., 2014), rodents (Kopec et al., 2015; Guo et al., 2017), and humans (Curtis and Lee, 2010; Sreenivasan et al., 2014). Classical experiments identified persistent stimulus-tuned activity in the prefrontal cortex of monkeys as a potential neural correlate of working memory (Fuster, 1973; Goldman-Rakic, 1995), while ramping activity in several cortical and subcortical regions has been linked to integration of noisy sensory evidence (Shadlen and Newsome, 2001; Yartsev et al., 2018). Although these processes have typically been studied separately, many ethological tasks, such as hunting and foraging, require both. Localizing these processes to specific neurons and circuits has proven challenging in complex vertebrate brains (Brody and Hanks, 2016; Wang, 2021; Gupta et al., 2024).

Here we show that activity in a set of local neurons in the fly navigation center exhibits dynamics consistent with both olfactory evidence integration and directional working memory. Activity of these neurons gradually ramped up when encountering repeated odor hits during foraging in a simulated turbulent plume. These dynamics could be fit with a linear filter with a half-width of ~9 seconds. These neurons also showed activity that outlasted the odor input by durations up to several seconds. Notably, this persistent activity was strongly correlated with persistent directional running on a trial-by-trial basis, and was not observed in a neighboring set of local neurons within the same brain structure. Optogenetic silencing of these neurons impaired behavior at low pulse numbers, and curtailed persistent directional running after odor offset. Our results thus strongly implicate VT062617 neurons as a specific locus for working memory and evidence accumulation.

Dominant models of working memory rely on attractors generated by recurrent excitatory connectivity (Brody et al., 2003; Zylberberg and Strowbridge, 2017; Wang, 2021). While optogenetic perturbation experiments have provided indirect evidence for recurrent attractor

networks (Wimmer et al., 2014; Kopec et al., 2015; Guo et al., 2017; Inagaki et al., 2019), direct evidence for these models has been challenging to obtain, given the distributed nature of vertebrate working memory circuitry (Khona and Fiete, 2022). The major local neuron type labeled by VT062617 has been identified as hΔK in the hemibrain connectome (Hamid et al., 2024), which shows strong recurrent connections with another CX cell type known as PFG (Hulse et al., 2021), although this line also labels at least one other type of local neuron. In contrast, 52G12 appears to label a large number of FC1 types (Supp. Fig. 5A), which represent one of the most direct feedforward pathways from input to output within the FB (Hulse et al., 2021). Future recording and perturbation experiments using more specific genetic labels should allow us to directly test whether the distinct dynamics of these two populations reflect their distinct circuit connectivities, or some other form of intrinsic or synaptic dynamics.

Intriguingly, we found that both VT062617 and 52G12 neurons showed slow modulation correlated with behavioral engagement in the navigation task. Working memory function in both humans and vertebrate models is known to depend on neuromodulatory tone (Cools and Arnsten, 2022). Different layers of the FB express characteristic neuromodulators and peptides (Nässel and Zandawala, 2019), which transcriptomics can link to specific neural subtypes (Epiney et al., 2023). Tangential input neurons to the FB have been shown to track and regulate internal states such as hunger and sleep need (Donlea et al., 2014; Flores-Valle and Seelig, 2023), and are well-poised anatomically to regulate activity in FB local neurons. We hypothesize that the slow variation we observe in both neural activity and behavior might reflect slowly changing neuromodulatory tone across the FB. In the future, the exquisite molecular control available in the fly should make it possible to directly test how peptides and modulators sculpt neural dynamics to adapt cognitive processing to state-dependent behavioral needs.

Allocentric goal representations for evidence accumulation during natural behavior

Recent studies of the FB suggest that it translates variables into allocentric coordinates (Lu et al., 2022; Lyu et al., 2022; Mussells-Pires et al., 2024; Westeinde et al., 2024), and can represent goal directions for navigation in this world-centric system (Mussells-Pires et al., 2024). However, many forms of navigation— such as pursuit of a visual target— can be accomplished through feedforward ego-centric steering (Semmelhack et al., 2014; Ribeiro et al., 2018). Why might the fly require an abstract or allocentric representation of its goal direction for olfactory navigation? Within a turbulent plume, odor concentration is generally a poor cue to source direction (Crimaldi and Koseff, 2001; Connor et al., 2018). Instead, behavioral experiments argue that insects integrate many different cues to navigate towards an odor source, including the temporal pattern of odor encounters (Mafra-Neto and Cardé, 1994), differences in odor concentration across the antennae (Borst and Heisenberg, 1982), the motion of the odor itself (Kadakia et al., 2022), and the direction of the wind (David et al., 1983). In flight, the computation of wind direction is complicated by the fact that extrinsic changes in wind cannot be observed directly from primary mechanosensors (van Breugel et al., 2022), further motivating the need for central computations to determine a goal direction. An allocentric representation of estimated source direction would allow the fly to weigh and accumulate evidence for or against

a particular direction in world coordinates, rather than having to update these representations with each turn. Given the ability of VT062617 neurons to enforce a goal direction (Matheson et al., 2022), and the slow and variable updating of bump position we observed here, we hypothesize that the bump we observe in VT062617 neurons might represent an internal estimate of odor source direction.

Understanding how different species represent goals for navigation remains an area of active research (Sarel et al., 2017; Basu et al., 2021; Ormond and O'Keefe, 2022). *Drosophila* larvae, which navigate in much more stable odor gradients (Gomez-Marin et al., 2011), lack a fully developed central complex (Andrade et al., 2019), and may require only egocentric computations to navigate. While allocentric representations of goal direction are now established in adult flies (Mussells-Pires et al., 2024), it remains unclear if the FB also encodes goal locations. A recent theoretical model has suggested that insects could use a pair of FB vectors, one pointed towards home, and one estimating a goal direction, to triangulate the location of a goal (Goulard et al., 2023). In contrast to flies, rodents foraging for odorous food rapidly switch from using odor cues to remembered spatial positions (Gire et al., 2016). In rodents performing odor-localization tasks, mixed odor and spatial representations develop at many places along the pathway from odor input to hippocampus (Poo et al., 2022). How the distinct navigation systems of vertebrates and invertebrates might enable different behaviors remains an open question (Basu and Nagel, 2024). Using ethological tasks to tease apart the nature and causal role of goal representations can provide insight into the structure and organization of navigation circuits across species.

Methods

1) Animals

Fly strains and husbandry

All flies were raised at room temp (approximately 24°-26°C) on a 12 hour light/dark cycle on standard cornmeal-agar food. For imaging experiments we used 7-12 day old female flies that were starved for ~24 hours. Experiments were run from 0-9 hours ZT. For freely walking wind tunnel experiments, we used 3-7 day old female flies. Flies were light shifted for at least three days and then starved for 18-24 hours before experimentation. For GtACR1 flies, fly food was supplemented with hydrated potato flakes containing all-trans-retinal (35mM stock: Sigma, R2500, dissolved in ethanol, stored at −20°C).

Genotypes used in each figure were as follows:

Figure 1-3, S1-4,6	VT062617-Gal4 > UAS-GCaMP7f,UAS-tdTomato
Figure 4, S5	52G12-Gal4 > UAS-GCaMP7f,UAS-tdTomato VT062617-Gal4 > UAS-GCaMP7f,UAS-tdTomato
Figure 5	w1118 5905 (6A-C) VT062617-Gal4 > UAS-GtACR1 (6D-H, S6A-D)

	Empty-Gal4>UAS-GtACR1 (6I-J, S6E-I)

2) Experimental Procedures:

Closed-loop olfactory navigation paradigm:

We designed a wind and odor delivery system in which the angular position of a wind tube and the status of a binary odor valve could be controlled in either open- or closed-loop by parameters of the fly's locomotion, as measured on an air-supported walking ball. Wind and odor delivery was accomplished via a rotary union (Dynamic Sealing Technologies, # LT-2141-OF-ES12-F1-F2-C2) with three isolated channels that allowed continuous rotation of wind and odor outputs while maintaining isolation and pressure. The three channels carried wind, odor, and compensatory air for the odor OFF condition so that equal airspeed was maintained with and without odor. Air to all lines first passed through a pressure regulator (Cole-Parmer MIR2NA), and charcoal filter (Drierite 26800 Drying column, with desiccant replaced by activated charcoal). The wind line was then humidified and passed through a mass flow controller (Aalborg Model GFC17), and set to one of three flow rates: 0.2, 0.4, or 0.6 L/min. Air to the odor (5% apple cider vinegar) and comp (humidified air) lines was set to a flow rate of 0.3 L/min using a flowmeter (Cole-Parmer PMK1-010608). Air from the wind and odor/comp lines were mixed in a customized 3D-printed chamber that led to a 3.5cm Teflon laminarizing tube (5mm ID) extending to 2 cm from the fly's antennae. Wind, comp, and odor entered the mixing chamber sequentially to prevent back flow of odor into clean air lines.

The wind ON condition was achieved by opening a solenoid valve (Cole-Parmer Masterflex P/N 01540-11) on the wind line and a high-speed three-way solenoid valve (Lee company, LHDA1233115HA) to divert air through the comp line rather than the odor line. In the ODOR ON condition air was instead diverted through the odor solution. All three valves were positioned immediately before the rotary union. Wind and odor lines were of Tygon tubing of either 1/16" ID or 1/8" ID.

Fly behavior was monitored using a lightweight walking ball (9 mm diameter General plastics FR-7110), supported by air from a custom 3D-printed holder. Airflow supporting the ball was controlled by a flow meter (Cole-Parmer PMK1-010608) at ~0.4 L/sec. The ball was painted with spots of black ink for tracking by the FicTrac sphere tracking software (Moore et al. 2014) using a Point Grey Camera (100 fps, Grasshopper, 94mm/0.5x InfiniStix Proximity Series lens, Edmund Optics Focal Length Extenders, working distance=15cm) and illuminated using two IR LED fiber optic cables (Thorlabs M118L03 flat cleave patch cables, M850F2 fiber coupled LEDs, and LEDD1B drivers). Two secondary cameras (30fps, FLIR Blackfly, Computar 8.5mm 1:1.3 adjustable lens) viewed the front and side of the fly for positioning.

The fly was held in place using a custom 3D-printed holder made of opaque resin (Grey Resin V5, Formlabs), with a tapered saline well that opens to a .9 x .9 mm imaging window at its nadir. Resin thickness around this window is necessarily thin (~25-50 microns) to accommodate the objective's working distance to the exposed brain below the window. The holder was held in place onto a fixed steel platform using a magnetic mount (Siskiyou MGB/20).

Closed-loop wind position from a walking ball

During closed-loop wind delivery, we used a microcontroller (TeensyDuino +USB) and stepper motor (Oriental PKP566FMN24A, with controller CVD524-K) to rotate the rotary union on which the wind tube was mounted, as shown in Figure 1A. The amount of rotation per 10ms interval was set to be equal to the rotation around the z axis of the walking ball. No additional filtering was performed to maximize motor responsiveness, but the motor controller filtered out some rapid changes, leading to small amounts of error accumulation (~0-90° per trial, depending on the amount of rapid turning). Therefore, an IR beam-break (Adafruit #2168) was used to reposition the wind at 0° from the front of the fly before each trial.

Functional imaging

All two-photon calcium imaging experiments were performed under a 20x water dipping objective (Olympus Plan Fluorite XLUMP 20x/1.0). The GCaMP7f calcium and tdTomato indicators were excited using an infrared laser (SpectraPhysics MaiTai HP) at 920nm at ~20-40mW of power at the sample. Emitted fluorescence was detected using GaAsP photomultiplier tubes, and separated using green (GCaMP7f, 525/50) and red (tdTomato, 607/70) bandpass filters. Images were collected using ThorLabs LS 3.0 software, where 3-4 optical sections (typically 122 x 74 μm imaging window) were taken 8-12μm apart in the z plane, all within the fan-shaped body (determined using the tdTom signal). Volumes were taken at 4-8 vol/s with a 1.2μs dwell time.

Software control

Control of wind speed, wind position, and wind/odor state were managed by custom Python software and integrated with Fictrac ball-tracking software using an interface adapted from Python Ball Motion Tracking software from the lab of Mala Murthy. A NiDAQ board (NI PCIe-6321) and breakout (NI BNC-2110) were used for data acquisition and communication between controllers as well as to send synchronization signals to the 2-photon microscope. Behavior data from the walking ball was collected and saved using the Fictrac image processing software at 100fps. The Fictrac timestamps (also at 100 fps) were used to trigger wind and odor changes (see experimental paradigms for timing) as well triggering 2-photon imaging (at 3s from the beginning of ball tracking).

Fly tethering and preparation

Flies were first anesthetized over ice in a glass scintillation vial for 5-10s, then held in a chilled aluminum “sarcophagus” (4-10°C) while being glued (McNett Aquaseal UV Fast Fix) into a custom 3D printed holder. Flies were only attached to the holder across the eyes and in front of the forelegs (episternum), so that the antennae and legs were clear and free to move. The head was tilted down to expose the back surface of the head in the saline well above. A minimal portion of this surface cuticle was removed directly above the FB to minimize tissue damage, prior to positioning the fly on the walking ball. Extracellular saline (103 mM NaCl, 3 mM KCl, 5 mM TES, 8 mM trehalose dihydrate, 10 mM glucose, 26 mM $NaHCO_3$, 1 mM $NaH_2PO_4H_20$, 1.5 mM $CaCl_22H_2O$, and 4 mM $MgCl_26H_2O$, pH 7.1–7.4, osmolarity 270–274 mOsm), bubbled with carbogen (5% CO_2, 95% O_2) and warmed to 33°C, was continuously perfused at ~1mL/m.

Experimental paradigms

Four types of experimental paradigms were used during imaging trials: 1) Closed-loop wind trials, where fly orientation was in constant control of the wind position and odor presentation was experimentally controlled , 2) open-loop wind trials (Fig. 2G-K), where the wind position was fixed in an experimentally set position (+/- 45°) and odor was experimentally controlled, and 3) wind-shift trials (Fig. 2C-F) where the wind position was transiently shifted during the odor period (+/- 90° at 45°/s) and, 4) plume trials (Fig. 3, Fig. 4F,G), where the wind direction was in closed loop with the animal orientation and odor was in closed-loop with fly position in a fictive 2D space (see Figure 3A).

For plume experiments, the state of the odor valve was determined by an adaptive compression algorithm acting on odor concentrations based on virtual movement through a turbulent plume.

At each frame, fly position in virtual x,y space was first determined from FicTrac monitoring of ball motion. Fly coordinates in x,y, and time were used to index into a previously recorded movie of a turbulent boundary layer acetone plume at 6mm above the bed in 10 cm/s wind recorded with a UV laser light sheet (Álvarez-Salvado et al., 2018; Connor et al., 2018). Plume concentrations were normalized such that the peak concentration was 1.

Instantaneous odor concentration values were fed into an adaptive compression algorithm based on previous studies of fly behavior (Álvarez-Salvado et al., 2018), and of temporal encoding at the olfactory periphery (Nagel and Wilson, 2011). Odor concentration at the ith frame C_i was first passed through a Hill function of the form

$$x_i = \frac{C_i}{C_i + A_i + \beta}$$

where $\beta = 0.025$ is the baseline threshold and A is an adaptation term the shifts the threshold to the right based on the recent history of odor exposures:

$$A_{i+1} = A_i + (C_i - A_i)/\tau$$

where $\tau = 500$ samples (equal to 5s at 100Hz). The odor valve was turned on when $x > 0.5$ and was off otherwise.

In all experiments, we first performed 5-20 50s trials of closed-loop wind with no 2-photon imaging to acclimatize the fly to closed-loop navigation paradigm. During these trials, where wind was on for the duration of the trial, odor was presented from 20-30s, and wind speed was randomly set to one of the 3 speed settings (16, 25, or 33 cm/s at the fly). After several trials, we examined behavior to see which speed was optimal for straight up-wind walking during odor and increased turning after odor offset. This speed was used for the remainder of experimental trials, although we sometimes adjusted wind speed in later trials if the fly walked less. We excluded flies that did not walk during at least 5 of these preliminary

trials. If no odor response was observed but the fly was walking well, flies were still included in the data set and the 25 cm/s wind speed was used.

For imaging trials, the closed-loop paradigm consisted of trial onset where wind position was set to a randomly at +/- 45, 135, or 0°. First the wind tube moved in closed-loop with the fly position without wind for 10s, then wind was presented at the determined speed for 15s. Odor was then presented with the wind for 15s, followed by 15s more of wind-only and 7s of no wind (total of 65s including the 3s pre-trigger time). Open-loop wind trials consisted of the same wind and odor timing, but with no wind-position movement during the trial. Each experiment consisted of 5-20 closed-loop wind trials, followed by interleaved, or alternating, open-loop and closed-loop trials for 10-30 more trials.

Experiments with plume trials also began with closed-loop speed-setting trials, followed by 10- 30 plume trials that were 100s long. The fly was positioned 140 fictive mm downwind from the midline of the plume source and oriented randomly at +/- 45, 135, or 0° at the beginning of each trail. All flies were allowed to walk freely in the plume space, with no intervention if they left the plume. In this case, the fly would not receive odor until it walked back into the plume. In one fly, plume trials were run after a set of interleaved closed-loop/open-loop trials.

Behavioral experiments in wind tunnels

Freely walking wind tunnel experiments were performed as described previously (Álvarez-Salvado et al., 2018; Matheson et al., 2022). Briefly, the position and orientation of walking flies were tracked in shallow acrylic arenas using IR LEDS (850 nm, Environmental Lights) and a camera (Basler acA1920-155um). Constant laminar airflow was maintained at ~12 cm/s. Odor pulses of 1% apple cider vinegar (Pastorelli) were delivered at 1 Hz (500 ms duration) using solenoid valves (LHDA1233115HA, Lee Company) mounted directly below the wind tunnel. For GtACR1 inactivation experiments, blue light was delivered using a panel of LEDs (470nm, Environmental Lights) at an intensity of 58 $\mu W/mm^2$ (measured at 530 nm). Flies were briefly anesthetized with ice for 30-60 seconds to load them into the wind tunnels.

3: Data Analysis

All analysis was performed in MATLAB (Mathworks, Natick, MA)

Processing of walking ball data

For walking ball data, angular velocity and forward velocity were calculated as the change in rotation of the ball around the z and x axes, respectively. For close-loop wind trials, heading was reported as the position of the wind tube, which was controlled by the change in z rotation, but would also account for any error in the control. Wind tube position was updated based on a running average of measured z-rotations over 10 samples at 100 samples/s. Z-rotations above 1000°/s were clipped. In open-loop trials, where wind position was fixed, heading was reported as the integrated change in z-rotation between frames of the ball at the current frame (Moore et al. 2014). For plotting and bump detection, heading, angular velocity,

and forward velocity signals were smoothed using a sliding averaging window of 50 frames (0.5s). For statistical tests (e.g. Fig. 1C, 2D, 3H) and linear filter calculations (Fig. 3E-G, 4B,C), we used unfiltered values as described above. Speed was calculated as the velocity in direction of heading based on the fictive fly path derived from integrating all three rotational velocities to map position on to a 2D plane (Moore et al., 2014). X and Y position of the fly were calculated as the cumulative sum of the speed multiplied by the sine or cosine, respectively, of heading. For plume trials, X and Y position values were calculated online to enable closed-loop odor control. Up-wind velocity was calculated as the cosine of heading multiplied by speed.

Processing of imaging data

For fluorescence extraction, all image volumes were first reduced to single planes as maximum intensity projections across each z plane. Maximum intensity projections were highly correlated with mean projections (Supp. Fig. 6), but had slightly higher signal-to-noise. We then concatenated projections for all trials of an experiment, and used the NoRMCorre algorithm (Pnevmatikakis et al., 2016) to correct for rigid motion across both red and green channels. We drew ROIs by hand in ImageJ, using a maximum intensity projection across all frames of a single trial (typically the first trial) on the red tdTOM channel. We then imported these ROIs into Matlab, and aligned them to subsequent images using register_rois2 (Giovannucci et al., 2019). For both VT062617 and 52G12 imaging, we drew ROIs for each of 8 putative columns in the dorsal layer of the FB. A baseline value for each ROI was calculated as the mean of the lowest 3% of fluorescent values across all trials. $\Delta F/F$ was then calculated by subtracting this baseline value from the green fluorescence values and dividing them by the baseline value. Fluorescence timeseries data was synchronized to the timestamps of behavior data using the 3s trigger time.

Analysis of neural encoding properties:

To detect activity bumps (e.g. Fig. 1E, H-L), we used a threshold-based algorithm, where the threshold for $\Delta F/F$ was set to 0.5 standard deviations above the mean $\Delta F/F$ of the entire experiment. A minimum bump duration was set at 5s and bumps with gaps <3s from a consecutive bump were merged. Using this detector, we classified samples of behavior data as bump or non-bump, and detected bump onset and offset times, which were used for bump-onset and offset triggered analysis (e.g. Fig. 1J, Supp. Fig. 4D).

Bump width (Fig. 1E, 4B) was computed by aligning each bump sample by the ROI with the peak $\Delta F/F$, and then wrapping the other ROI values to the 8 column space using the modulus function in Matlab. Aligned bumps were averaged across trials and flies. Only flies with bumps in at least 2 trials for each condition were kept (N=14).

Bump offset delays (Fig. 1H, Supp. Fig. 1E) were calculated by subtracting the odor offset time from the bump offset time in all bumps that began during the odor period and ended at least one second before the odor offset time. Only flies were included that had at least 5 bumps meeting this requirement for fly means (Fig. 1H). All bumps were also pooled across all flies (Supp. Fig. 1E).

Straightness (Fig. 1I, Supp. Fig. 5E) was computed as the ratio of displacement (the distance of a straight line from the beginning and end points of a window) to path length (the

sum of all displacements within the window) over a sliding 1.5s window. This value was then squared. To include shorter bumps and exclude periods of low bump amplitude in this analysis, the gap threshold of the bump detector was lowered to <3s and minimum bump length raised to >5s for analysis. Only flies with more than 2 trials with bumps in each period were included. The same bump criteria were applied for angular speed in Supp. Fig. 5E)

For bump offset and onset analysis (Fig. 1J,K, Supp. Fig. 1F, Supp, Fig. 4D), locomotor data were aligned to the transition from bump ON to bump OFF for each bump that began during the odor period or wind period before odor. Only flies with more than 2 trials with such bumps were included. An additional behavior metric, goal-direction deviation ($|\theta-\theta_{goal}|$) was calculated by subtracting the current heading from the goal heading (θ_{goal}), defined as the mean heading during the odor period, and finding the absolute value of those values. For this analysis, bump and behavior metrics were smoothed with a 1s sliding window before taking means. For statistical comparisons of changes before and after bump times, means of activity were calculated for each bump in defined time windows relative to the bump offset or onset time. For offset associated measures, angular velocity measurements were averaged from 4 to 1s before bump offset and from 2 to 5s after. Heading deviation comparisons were all made from averages between 4 to 1s before offset and 5 to 8s after (Fig. 1J, Supp. Fig. 1F, blue boxes). For onset measures, mean forward velocity was compared from a window -7 to -4 s before onset to a window -1.5 to 1.5 s from onset. A paired two-sample t-test was used for all comparisons.

The post-odor goal vector sum (Fig. 1L) was calculated for each bump that extended past the odor offset time, only for the period after odor offset. The vector was calculated by taking a histogram of the orientation values during this post-odor period, converting the histogram into cartesian coordinates, summing the histogram to get a single vector, and then projecting this vector onto the goal direction. This value was compared the same vector calculation for a period of equal duration after bump offset. Examples of how this vector captures goal-directed movement as opposed to less directed movement or movement directed in a non-goal direction are shown in Supp. Fig. 1H.

For bump position analyses (Fig. 2A,B,E-H,J,K, Supp. Fig. 2), we smoothed the extracted fluorescence traces using a 1s sliding window in the time domain and a two-column window in the spatial domain, then computed bump position as the maximum ROI (or FB column) for each sample where a bump was detected using our bump finder algorithm above. Positions were then unwrapped to show absolute column shifts. We computed correlations between bump position and heading for all bump instances (Fig. 2B top) and averaged across each fly with bump activity in at least 5 trials (Fig. 2B bottom) using Pearson's correlation coefficient.

For wind-shift analysis (Fig. 2C-F), we analyzed only trials in which a bump was present before and during the shift. Wind driven heading shifts were detected when mean angular velocity during or up to 2s after the shift was greater than a time window of equal duration before the shift. Heading and position for right shifts were multiplied by -1 so all shifts could be directly compared on the same axes. Heading and bump position were both converted to degrees to facilitate comparison. Displacements were calculated over time windows 2s before and after the wind shift onset.

For open-loop wind trials (Fig. 2G-K), we analyzed turning responses in all flies with at least two open-loop trials (N=12 flies). We analyzed bump movement (Fig. 2J) in flies where at least four of these open-loop trials showed bump activity (N=9) and compared bump displacement (in columns) during the odor period in open-loop trials to closed-loop trials from the same flies. To quantify displacement gains (Fig. 2K), we pooled all bumps for each trial type and computed bump and heading displacement means. We fit a line (Matlab's polyfit) to each trial type to determine average gain. We also calculated gains for each bump by dividing each total bump displacement by heading displacement over that same time period to see distribution across flies (Supp. Fig. 2A).

For slow-time scale analysis (Fig. 4D,E, Supp. Fig. 5F), we measured various behavioral metrics (upwind velocity, probability of movement, and forward velocity) during the odor period for each trial. Probability of movement is a binarized movement state where any sample with an instantaneous forward velocity greater than 2 mm/s is set to 1. We then computed Pearson's correlation coefficient between these metrics and the mean $\Delta F/F$ for the same periods and trials. To assess significance, we compare these to correlation coefficients between metrics and $\Delta F/F$ for shuffled trials (null condition).

To analyze encoding of odor dynamics during plume experiments (Fig. 3D and Supp. Fig. 3B), we computed instantaneous odor frequency (Demir et al., 2020) by convolving the binary odor signal with an exponential filter with a timescale τ=2s. For every odor encounter, we then found $\Delta F/F$ and odor frequency at 5 time periods from 0 to 20s from the end of that encounter. Only encounters where no future encounter occurs before the given time delay were included in each plot.

To compute linear filters relating odor experience and locomotor parameters to neural activity (Fig. 3E-G, Fig. 4B,C, Supp. Fig. 4A-C), we first computed bump amplitude, forward velocity, and angular velocity as described above. The first 400 samples of each trace were discarded as the bump amplitude typically contained an artifact due to shutter opening. The remaining traces were concatenated to form a single vector for each parameter and all traces were mean subtracted. Forward velocity and absolute angular velocity were normalized to have unit standard deviation. We then computed the cross-correlogram between bump amplitude and odor, forward velocity, and absolute angular velocity in the frequency domain.

To account for correlations between odor and locomotor parameters, we adapted Methods described in Nagel and Doupe 2008 to account for correlations between odor, forward velocity, and angular velocity. Briefly, we computed the complex autocorrelation matrix A at each of 256 frequencies from 0.2 to 5 Hz of the odor o(t), forward velocity f(t), and absolute angular velocity a(t) traces:

$$A_\omega = \tilde{S}'_\omega \tilde{S}_\omega$$

where

$$S_\omega = [\overrightarrow{o_\omega} \quad \overrightarrow{f_\omega} \quad \overrightarrow{a_\omega}]$$

We then computed the pseudo-inverse of A for each frequency ω by taking the singular value decomposition:

$$U\Sigma V' = A_\omega$$

and inverting the diagonal terms of Σ with a regularization parameter λ that was set to 0.0001.

$$\Sigma_{inv}(s,s) = \frac{1}{\Sigma(\mathrm{s},\mathrm{s})} + \lambda$$

The decorrelated filter was equal to:

$$\widetilde{D} = V\Sigma_{inv}U'\tilde{C}$$

Where $\tilde{C}$ is the Fourier transform of the raw cross-correlogram for each parameter:

$$C_\omega = [\overrightarrow{C_{o\omega}} \quad \overrightarrow{C_{f\omega}} \quad \overrightarrow{C_{a\omega}}]$$

To compare filters from different fly lines (Fig. 4B,C), we normalized all filters by dividing by the standard deviation of the filter and subtracting minimum standard deviation values. To compare half-widths of filters, we first smoothed each filter using a sliding window of 1s. We then found the half-prominence width of peaks determined as local maxima where the prominence was a minimum of 1.5 times the mean for each fly (Matlab findpeak function, with defined prominence properties). To compare angular velocity filters, we found the area under the curve for each fly using a trapezoidal estimation for each data point (Matlab trapz function).

Analysis of freely walking wind tunnel behavior data:

Freely walking behavioral data were preprocessed as described previously (Álvarez-Salvado et al., 2018; Matheson et al., 2022): trials with less than 25 mm of movement were excluded, and position and orientation raw data were low pass filtered at 2.5 Hz. As upwind walking could persist if a fly tracks the arena walls, we further filtered our data by excluding data points where the fly's position was within 3 mm of a wall.

Upwind walking probability was determined by binarizing the orientation data depending on if the orientations were inside or outside of a 90° cone, and whether the flies were walking above or below 0.5 mm/s. This binarized data was further processed in three ways to evaluate persistence and evidence accumulation. First, the binarized data were averaged at each timepoint to compute the upwind walking probability over time (Fig. 5B,D,E). Second, the upwind walking probabilities over time were averaged between 2 s and 6 s following odor onset to compute peak responses (Fig. 5C,G,I). Third, the binarized data between 0 and 10 s

following odor offset were averaged across trials for each fly to compute post-odor upwind orientation probabilities (Fig. 5F,H).

4: Key Resources Table

Resource	Source	Identifier
FLY LINES		
VT062617-Gal4	VDRC	VDRC: 206875
52G12-Gal4	BDSC	RRID: BDSC_49581
Empty-Gal4	BDSC	RRID: BDSC_68384
w^{1118} 5905	Alvarez-Salvado et al. 2018	
UAS-GCaMP7f,UAS-tdTomato	BDSC/Nagel lab	RRID: BDSC_80906, 36327
w^{1118},s/CyO;UAS-GtACR1-EYFP/TM6b	Claude Desplan	
SOFTWARE		
Python		Version 3.8
MATLAB	Mathworks	Version R2023a
Image J		Version 1.53t
FicTrac		Version 2.0 (build date: Nov 2 2018)
Pybmt	Mala Murthy lab	
CalmAn		
Register_roi2	Jason Moore	

Acknowledgements

The authors would like to thank Mala Murthy and her lab for providing modified FicTrac code (Pybmt) and advice on closed-loop behavior, John Crimaldi and his lab for plume data, and Margot Elmaleh in Michael Long's lab for advice on 3D printing. Claude Desplan's lab provided GtACR1 flies. David Schoppik provided assistance with 2-photon microscopy. Christina May generated imaging stocks and provided support for 2-photon microscopy. Emily Hao provided assistance with behavioral experiments. Jason Moore provided assistance with imaging analysis. Jonathan Victor provided advice on regularizing the filter decorrelation. Michael Long, Jonathan Victor, Floris van Breugel, and members of the Nagel and Schoppik labs provided input on the manuscript. This work was supported by NINDS Brain Initiative NS127129, NIDCD DC017979, and NSF 2014217 Odor2Action to K.I.N.

Author Contributions

N.D.K. and K.I.N designed the study. N.D.K. developed the closed-loop wind and odor apparatus, developed all all hardware and software related to the apparatus, and collected and

analyzed all behavior and imaging data using this apparatus. A.J.L designed, ran, and analyzed freely walking behavioral data and developed the goal vector sum analysis. K.I.N. wrote code for the filter anlaysis. J.D.F. obtained confocal data. N.D.K. and K.I.N. wrote the paper with input from A.J.L.

References

Ackels T, Erskine A, Dasgupta D, Marin AC, Warner TPA, Tootoonian S, Fukunaga I, Harris JJ, Schaefer AT. 2021. Fast odour dynamics are encoded in the olfactory system and guide behaviour. *Nature* **593**(7860): 558–563. doi: 10.1038/s41586-021-03514-2

Álvarez-Salvado E, Licata AM, Connor EG, McHugh MK, King BM, Stavropoulos N, Victor JD, Crimaldi JP, Nagel KI. 2018. Elementary sensory-motor transformations underlying olfactory navigation in walking fruit-flies. *Elife* **7**: e37815. doi: 10.7554/elife.37815

Andrade IV, Riebli N, Nguyen B-CM, Omoto JJ, Cardona A, Hartenstein V. 2019. Developmentally Arrested Precursors of Pontine Neurons Establish an Embryonic Blueprint of the Drosophila Central Complex. *Curr Biol* **29**(3): 412-425.e3. doi: 10.1016/j.cub.2018.12.012

Aso Y, Yamada D, Bushey D, Hibbard KL, Sammons M, Otsuna H, Shuai Y, Hige T. 2023. Neural circuit mechanisms for transforming learned olfactory valences into wind-oriented movement. *eLife* **12**: e85756. doi: 10.7554/elife.85756

Baker KL, Dickinson M, Findley TM, Gire DH, Louis M, Suver MP, Verhagen JV, Nagel KI, Smear MC. 2018. Algorithms for Olfactory Search across Species. *J Neurosci* **38**(44): 9383–9389. doi: 10.1523/jneurosci.1668-18.2018

Basu J, Nagel KI. 2024. Neural circuits for goal-directed navigation across species. *TINS*, in press.

Basu R, Gebauer R, Herfurth T, Kolb S, Golipour Z, Tchumatchenko T, Ito HT. 2021. The orbitofrontal cortex maps future navigational goals. *Nature* **599**(7885): 449–452. doi: 10.1038/s41586-021-04042-9

Boie SD, Connor EG, McHugh M, Nagel KI, Ermentrout GB, Crimaldi JP, Victor JD. 2018. Information-theoretic analysis of realistic odor plumes: What cues are useful for determining location? *PLoS Comput Biol* **14**(7): e1006275. doi: 10.1371/journal.pcbi.1006275

Borst A, Heisenberg M. 1982. Osmotropotaxis inDrosophila melanogaster. *J Comp Physiol* **147**(4): 479–484. doi: 10.1007/bf00612013

Brody CD, Hanks TD. 2016. Neural underpinnings of the evidence accumulator. *Curr Opin Neurobiol* **37**: 149–157. doi: 10.1016/j.conb.2016.01.003

Brody CD, Romo R, Kepecs A. 2003. Basic mechanisms for graded persistent activity: discrete attractors, continuous attractors, and dynamic representations. *Curr Opin Neurobiol* **13**(2): 204–211. doi: 10.1016/s0959-4388(03)00050-3

Connor EG, McHugh MK, Crimaldi JP. 2018. Quantification of airborne odor plumes using planar laser-induced fluorescence. *Exp Fluids* **59**(9): 137. doi: 10.1007/s00348-018-2591-3

Cools R, Arnsten AFT. 2022. Neuromodulation of prefrontal cortex cognitive function in primates: the powerful roles of monoamines and acetylcholine. *Neuropsychopharmacology* **47**(1): 309–328. doi: 10.1038/s41386-021-01100-8

Crimaldi JP, Koseff JR. 2001. High-resolution measurements of the spatial and temporal scalar structure of a turbulent plume. *Exp Fluids* **31**(1): 90–102. doi: 10.1007/s003480000263

Curtis CE, Lee D. 2010. Beyond working memory: the role of persistent activity in decision making. *Trends Cogn Sci* **14**(5): 216–222. doi: 10.1016/j.tics.2010.03.006

David CT, Kennedy JS, Ludlow AR. 1983. Finding of a sex pheromone source by gypsy moths released in the field. *Nature* **303**(5920): 804–806. doi: 10.1038/303804a0

Dekker T, Cardé RT. 2011. Moment-to-moment flight manoeuvres of the female yellow fever mosquito (Aedes aegypti L.) in response to plumes of carbon dioxide and human skin odour. *J Exp Biol* **214**(20): 3480–3494. doi: 10.1242/jeb.055186

Demir M, Kadakia N, Anderson HD, Clark DA, Emonet T. 2020. Walking Drosophila navigate complex plumes using stochastic decisions biased by the timing of odor encounters. *eLife* **9**: e57524. doi: 10.7554/elife.57524

Donlea JM, Pimentel D, Miesenböck G. 2014. Neuronal Machinery of Sleep Homeostasis in Drosophila. *Neuron* **81**(4): 860–872. doi: 10.1016/j.neuron.2013.12.013

Epiney D, Chaya GNM, Dillon NR, Lai S-L, Doe CQ. 2023. Transcriptional complexity in the insect central complex: single nuclei RNA sequencing of adult brain neurons derived from type 2 neuroblasts. *bioRxiv*: 2023.12.10.571022. doi: 10.1101/2023.12.10.571022

Flores-Valle A, Seelig JD. 2023. Dynamics of sleep and feeding homeostasis in Drosophila glia and neurons. *bioRxiv*: 2022.07.07.499175. doi: 10.1101/2022.07.07.499175

Funahashi S, Bruce CJ, Goldman-Rakic PS. 1989. Mnemonic coding of visual space in the monkey's dorsolateral prefrontal cortex. *J Neurophysiol* **61**(2): 331–349. doi: 10.1152/jn.1989.61.2.331

Fuster JM. 1973. Unit activity in prefrontal cortex during delayed-response performance: neuronal correlates of transient memory. *J Neurophysiol* **36**(1): 61–78. doi: 10.1152/jn.1973.36.1.61

Gattuso H, Nuñez K, Rea B de la, Ermentrout B, Victor J, Nagel K. 2024. Inhibitory control of locomotor statistics in walking Drosophila. *bioRxiv*: 2024.04.15.589655. doi: 10.1101/2024.04.15.589655

Giovannucci A, Friedrich J, Gunn P, Kalfon J, Brown BL, Koay SA, Taxidis J, Najafi F, Gauthier JL, Zhou P, et al. 2019. CaImAn an open source tool for scalable calcium imaging data analysis. *eLife* **8**: e38173. doi: 10.7554/elife.38173

Gire DH, Kapoor V, Arrighi-Allisan A, Seminara A, Murthy VN. 2016. Mice Develop Efficient Strategies for Foraging and Navigation Using Complex Natural Stimuli. *Curr Biol* **26**(10): 1261–1273. doi: 10.1016/j.cub.2016.03.040

Goldman-Rakic PS. 1995. Cellular basis of working memory. *Neuron* **14**(3): 477–485. doi: 10.1016/0896-6273(95)90304-6

Gomez-Marin A, Stephens GJ, Louis M. 2011. Active sampling and decision making in Drosophila chemotaxis. *Nat Commun* **2**(1): 441. doi: 10.1038/ncomms1455

Goulard R, Heinze S, Webb B. 2023. Emergent spatial goals in an integrative model of the insect central complex. *PLOS Comput Biol* **19**(12): e1011480. doi: 10.1371/journal.pcbi.1011480

Gray JM, Hill JJ, Bargmann CI. 2005. A circuit for navigation in Caenorhabditis elegans. *Proc Natl Acad Sci* **102**(9): 3184–3191. doi: 10.1073/pnas.0409009101

Guo ZV, Inagaki HK, Daie K, Druckmann S, Gerfen CR, Svoboda K. 2017. Maintenance of persistent activity in a frontal thalamocortical loop. *Nature* **545**(7653): 181–186. doi: 10.1038/nature22324

Gupta D, Kopec CD, Bondy AG, Luo TZ, Elliott VA, Brody CD. 2024. A multi-region recurrent circuit for evidence accumulation in rats. *bioRxiv*: 2024.07.08.602544. doi: 10.1101/2024.07.08.602544

Hamid A, Gattuso H, Caglar AN, Pillai M, Steele T, Gonzalez A, Nagel K, Syed MH. 2024. The conserved RNA-binding protein Imp is required for the specification and function of olfactory navigation circuitry in Drosophila. *Curr Biol* **34**(3): 473-488.e6. doi: 10.1016/j.cub.2023.12.020

Handler A, Graham TGW, Cohn R, Morantte I, Siliciano AF, Zeng J, Li Y, Ruta V. 2019. Distinct Dopamine Receptor Pathways Underlie the Temporal Sensitivity of Associative Learning. *Cell* **178**(1): 60-75.e19. doi: 10.1016/j.cell.2019.05.040

Hulse BK, Haberkern H, Franconville R, Turner-Evans D, Takemura S, Wolff T, Noorman M, Dreher M, Dan C, Parekh R, et al. 2021. A connectome of the Drosophila central complex reveals network motifs suitable for flexible navigation and context-dependent action selection. *eLife* **10**: e66039. doi: 10.7554/elife.66039

Inagaki HK, Fontolan L, Romani S, Svoboda K. 2019. Discrete attractor dynamics underlies persistent activity in the frontal cortex. *Nature* **566**(7743): 212–217. doi: 10.1038/s41586-019-0919-7

Kadakia N, Demir M, Michaelis BT, DeAngelis BD, Reidenbach MA, Clark DA, Emonet T. 2022. Odour motion sensing enhances navigation of complex plumes. *Nature* **611**(7937): 754–761. doi: 10.1038/s41586-022-05423-4

Khona M, Fiete IR. 2022. Attractor and integrator networks in the brain. *Nat Rev Neurosci* **23**(12): 744–766. doi: 10.1038/s41583-022-00642-0

Kopec CD, Erlich JC, Brunton BW, Deisseroth K, Brody CD. 2015. Cortical and Subcortical Contributions to Short-Term Memory for Orienting Movements. *Neuron* **88**(2): 367–377. doi: 10.1016/j.neuron.2015.08.033

Li F, Lindsey JW, Marin EC, Otto N, Dreher M, Dempsey G, Stark I, Bates AS, Pleijzier MW, Schlegel P, et al. 2020. The connectome of the adult Drosophila mushroom body provides insights into function. *eLife* **9**: e62576. doi: 10.7554/elife.62576

Lu J, Behbahani AH, Hamburg L, Westeinde EA, Dawson PM, Lyu C, Maimon G, Dickinson MH, Druckmann S, Wilson RI. 2022. Transforming representations of movement from body- to world-centric space. *Nature* **601**(7891): 98–104. doi: 10.1038/s41586-021-04191-x

Lyu C, Abbott LF, Maimon G. 2022. Building an allocentric travelling direction signal via vector computation. *Nature* **601**(7891): 92–97. doi: 10.1038/s41586-021-04067-0

Mafra-Neto A, Cardé RT. 1994. Fine-scale structure of pheromone plumes modulates upwind orientation of flying moths. *Nature* **369**(6476): 142–144. doi: 10.1038/369142a0

Matheson AMM, Lanz AJ, Medina AM, Licata AM, Currier TA, Syed MH, Nagel KI. 2022. A neural circuit for wind-guided olfactory navigation. *Nat Commun* **13**(1): 4613. doi: 10.1038/s41467-022-32247-7

Moore RJD, Taylor GJ, Paulk AC, Pearson T, Swinderen B van, Srinivasan MV. 2014. FicTrac: A visual method for tracking spherical motion and generating fictive animal paths. *J Neurosci Methods* **225**: 106–119. doi: 10.1016/j.jneumeth.2014.01.010

Mussells-Pires P, Zhang L, Parache V, Abbott LF, Maimon G. 2024. Converting an allocentric goal into an egocentric steering signal. *Nature* **626**(8000): 808–818. doi: 10.1038/s41586-023-07006-3

Nagel KI, Doupe AJ. 2008. Organizing Principles of Spectro-Temporal Encoding in the Avian Primary Auditory Area Field L. *Neuron* **58**(6): 938–955. doi: 10.1016/j.neuron.2008.04.028

Nagel KI, Wilson RI. 2011. Biophysical mechanisms underlying olfactory receptor neuron dynamics. *Nat Neurosci* **14**(2): 208–216. doi: 10.1038/nn.2725

Nässel DR, Zandawala M. 2019. Recent advances in neuropeptide signaling in Drosophila, from genes to physiology and behavior. *Prog Neurobiol* **179**(Arch. Insect. Biochem. Physiol. 74 2010): 101607. doi: 10.1016/j.pneurobio.2019.02.003

Ormond J, O'Keefe J. 2022. Hippocampal place cells have goal-oriented vector fields during navigation. *Nature* **607**(7920): 741–746. doi: 10.1038/s41586-022-04913-9

Pnevmatikakis EA, Soudry D, Gao Y, Machado TA, Merel J, Pfau D, Reardon T, Mu Y, Lacefield C, Yang W, et al. 2016. Simultaneous Denoising, Deconvolution, and Demixing of Calcium Imaging Data. *Neuron* **89**(2): 285–299. doi: 10.1016/j.neuron.2015.11.037

Poo C, Agarwal G, Bonacchi N, Mainen ZF. 2022. Spatial maps in piriform cortex during olfactory navigation. *Nature* **601**(7894): 595–599. doi: 10.1038/s41586-021-04242-3

Ribeiro IMA, Drews M, Bahl A, Machacek C, Borst A, Dickson BJ. 2018. Visual Projection Neurons Mediating Directed Courtship in Drosophila. *Cell* **174**(3): 607-621.e18. doi: 10.1016/j.cell.2018.06.020

Riffell JA, Shlizerman E, Sanders E, Abrell L, Medina B, Hinterwirth AJ, Kutz JN. 2014. Flower discrimination by pollinators in a dynamic chemical environment. *Science* **344**(6191): 1515–1518. doi: 10.1126/science.1251041

Sarel A, Finkelstein A, Las L, Ulanovsky N. 2017. Vectorial representation of spatial goals in the hippocampus of bats. *Science* **355**(6321): 176–180. doi: 10.1126/science.aak9589

Scaplen KM, Talay M, Fisher JD, Cohn R, Sorkaç A, Aso Y, Barnea G, Kaun KR. 2021. Transsynaptic mapping of Drosophila mushroom body output neurons. *eLife* **10**: e63379. doi: 10.7554/elife.63379

Seelig JD, Jayaraman V. 2015. Neural dynamics for landmark orientation and angular path integration. *Nature* **521**(7551): 186–191. doi: 10.1038/nature14446

Semmelhack JL, Donovan JC, Thiele TR, Kuehn E, Laurell E, Baier H. 2014. A dedicated visual pathway for prey detection in larval zebrafish. *eLife* **3**: e04878. doi: 10.7554/elife.04878

Shadlen MN, Newsome WT. 2001. Neural Basis of a Perceptual Decision in the Parietal Cortex (Area LIP) of the Rhesus Monkey. *J Neurophysiol* **86**(4): 1916–1936. doi: 10.1152/jn.2001.86.4.1916

Sreenivasan KK, Curtis CE, D'Esposito M. 2014. Revisiting the role of persistent neural activity during working memory. *Trends Cogn Sci* **18**(2): 82–89. doi: 10.1016/j.tics.2013.12.001

Stone T, Webb B, Adden A, Weddig NB, Honkanen A, Templin R, Wcislo W, Scimeca L, Warrant E, Heinze S. 2017. An Anatomically Constrained Model for Path Integration in the Bee Brain. *Curr Biol* **27**(20): 3069-3085.e11. doi: 10.1016/j.cub.2017.08.052

van Breugel F, Dickinson MH. 2014. Plume-Tracking Behavior of Flying Drosophila Emerges from a Set of Distinct Sensory-Motor Reflexes. *Curr Biol* **24**(3): 274–286. doi: 10.1016/j.cub.2013.12.023

van Breugel F, Jewell R, Houle J. 2022. Active anemosensing hypothesis: how flying insects could estimate ambient wind direction through sensory integration and active movement. *J R Soc Interface* **19**(193): 20220258. doi: 10.1098/rsif.2022.0258

Verano KVB, Panizon E, Celani A. 2023. Olfactory search with finite-state controllers. *Proc Natl Acad Sci* **120**(34): e2304230120. doi: 10.1073/pnas.2304230120

Victor JD, Boie SD, Connor EG, Crimaldi JP, Ermentrout GB, Nagel KI. 2019. Olfactory Navigation and the Receptor Nonlinearity. *J Neurosci* **39**(19): 3713–3727. doi: 10.1523/jneurosci.2512-18.2019

Wang X-J. 2021. 50 years of mnemonic persistent activity: quo vadis? *Trends Neurosci* **44**(11): 888–902. doi: 10.1016/j.tins.2021.09.001

Westeinde EA, Kellogg E, Dawson PM, Lu J, Hamburg L, Midler B, Druckmann S, Wilson RI. 2024. Transforming a head direction signal into a goal-oriented steering command. *Nature* **626**(8000): 819–826. doi: 10.1038/s41586-024-07039-2

Wimmer K, Nykamp DQ, Constantinidis C, Compte A. 2014. Bump attractor dynamics in prefrontal cortex explains behavioral precision in spatial working memory. *Nat Neurosci* **17**(3): 431–439. doi: 10.1038/nn.3645

Yartsev MM, Hanks TD, Yoon AM, Brody CD. 2018. Causal contribution and dynamical encoding in the striatum during evidence accumulation. *eLife* **7**: e34929. doi: 10.7554/elife.34929

Zolin A, Cohn R, Pang R, Siliciano AF, Fairhall AL, Ruta V. 2021. Context-dependent representations of movement in Drosophila dopaminergic reinforcement pathways. *Nat Neurosci* **24**(11): 1555–1566. doi: 10.1038/s41593-021-00929-y

Zylberberg J, Strowbridge BW. 2017. Mechanisms of Persistent Activity in Cortical Circuits: Possible Neural Substrates for Working Memory. *Annu Rev Neurosci* **40**(1): 603–627. doi: 10.1146/annurev-neuro-070815-014006

Figure 1

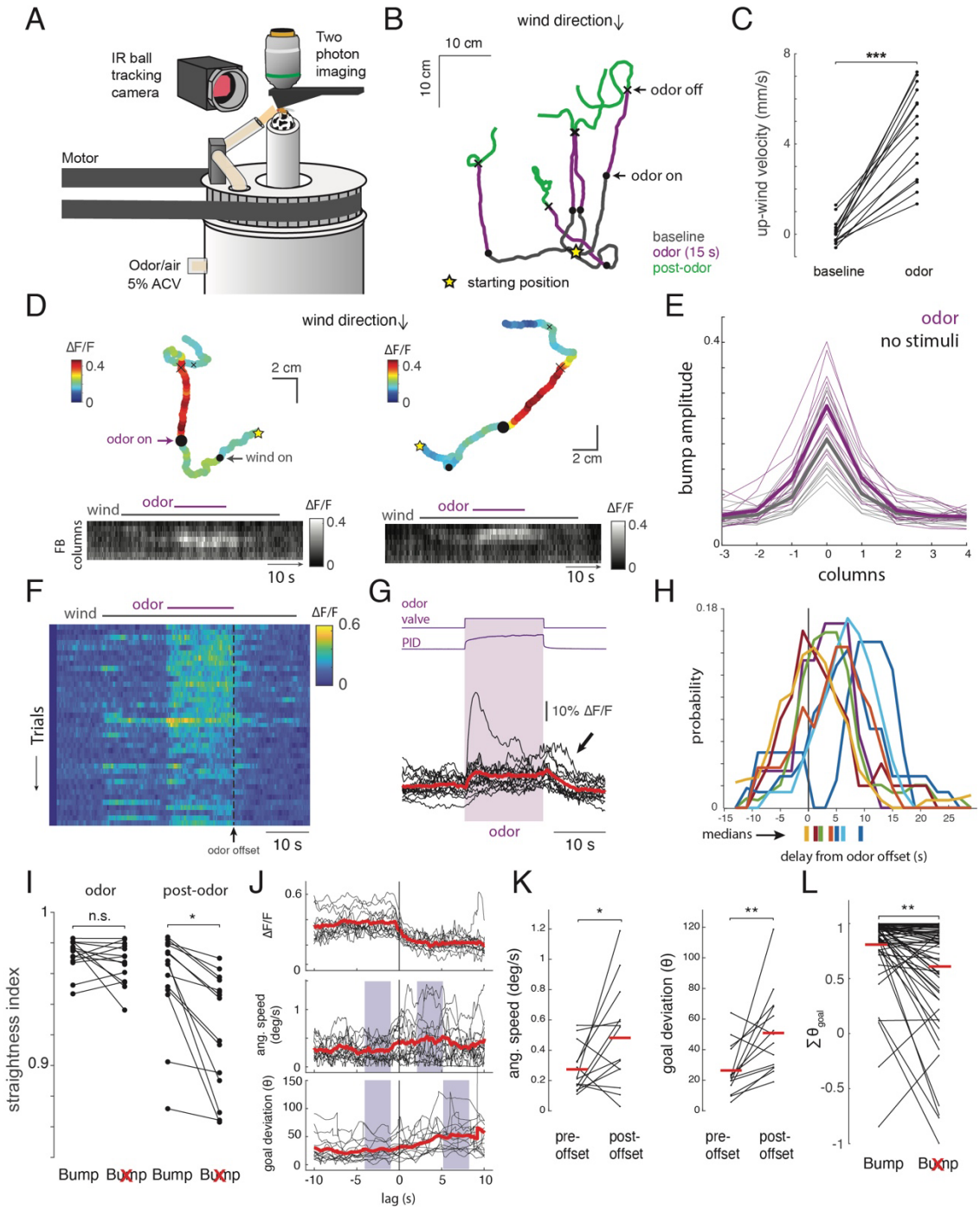

Figure 1: Persistent odor-evoked activity in VT062617 FB local neurons is associated with persistent goal-directed walking. A: Schematic of the preparation. A head-fixed fly walking on an air-supported ball can control wind direction (through a motorized rotary union) and odor (apple cider vinegar 5%) in open- or closed-loop. An IR camera tracks ball rotations. A 2-photon microscope images concurrent neural activity. B: Example trajectories from one fly performing closed-loop wind navigation in response to a 15s odor pulse. Odor evokes straight and generally upwind trajectories. Yellow star: starting position, circles: odor ON, X's: odor

OFF. C: Mean upwind velocities of N=15 flies expressing GCaMP in VT062617 neurons are higher during odor than at baseline period (paired t-test, p =0.001). D: Examples of VT062617 activity during closed-loop wind with an odor pulse. Top: virtual 2D trajectories with respect to wind direction (from top), color-coded by bump amplitude (max $\Delta F/F$ across columns). Small circles: wind ON, large circles: odor ON, large Xs: odor OFF, small xs: wind OFF. Note strongest activity during odor. Bottom shows activity across FB columns as a function of time. Wind and odor periods indicated above heatmaps. Odor drives a bump of activity limited to a few columns. E: Mean bump profile across columns. Thin lines represent mean across trials (9 to 52 trials for each fly) and thick lines represent mean across flies (N=14 flies with both odor and no-stimulus imaging data). F. Bump amplitude as a function of time for one fly. Note robust responses to odor with variable timing, and more variable and transient responses to wind ON. G. Mean timecourse of activity relative to measured odor timecourse (purple box). Black: mean for each fly (n=13-39 trials), red: mean across flies (N=14 flies). Note activity following odor OFF (black arrow). H: Distribution of bump offset times relative to odor offset for 7 flies in which we recorded at least 5 bumps that occurred during the odor period. Black line at 0 represents odor offset time as measured by PID. Median offset times shown below graph for each fly. I: Trajectory straightness (see Methods) in the presence vs absence of an activity bump for both odor and post-odor periods (N=14 flies). Mean straightness during odor did not differ between samples with and without a bump across flies (paired t-test, p=0.26), while straightness in the post-odor period was higher for samples with a bump (p=0.02). J: Analysis of locomotor features relative to bump OFF. Black traces show mean bump amplitude (top), angular speed (middle), and goal-direction deviation (bottom, see Methods) for each fly (n=9-39 trials per fly). Red traces represent means across flies (N=14 flies). K. Both angular speed (left) and deviation from goal direction (right) increase significantly after bump OFF (time periods compared shown by blue boxes in J, paired t-test, avel: p=0.043, goal dev.: p=0.008, see also Supp. Fig. 1F). L: Projection of fly heading onto goal direction during the post-odor period (see Methods, Supp Fig. 2D) is higher while the bump is ON than while the bump is OFF (n=64 trials from N=15 flies, paired t-test: p=0.007, bump mean=0.81, no bump mean=0.61).

Supp Fig. 1

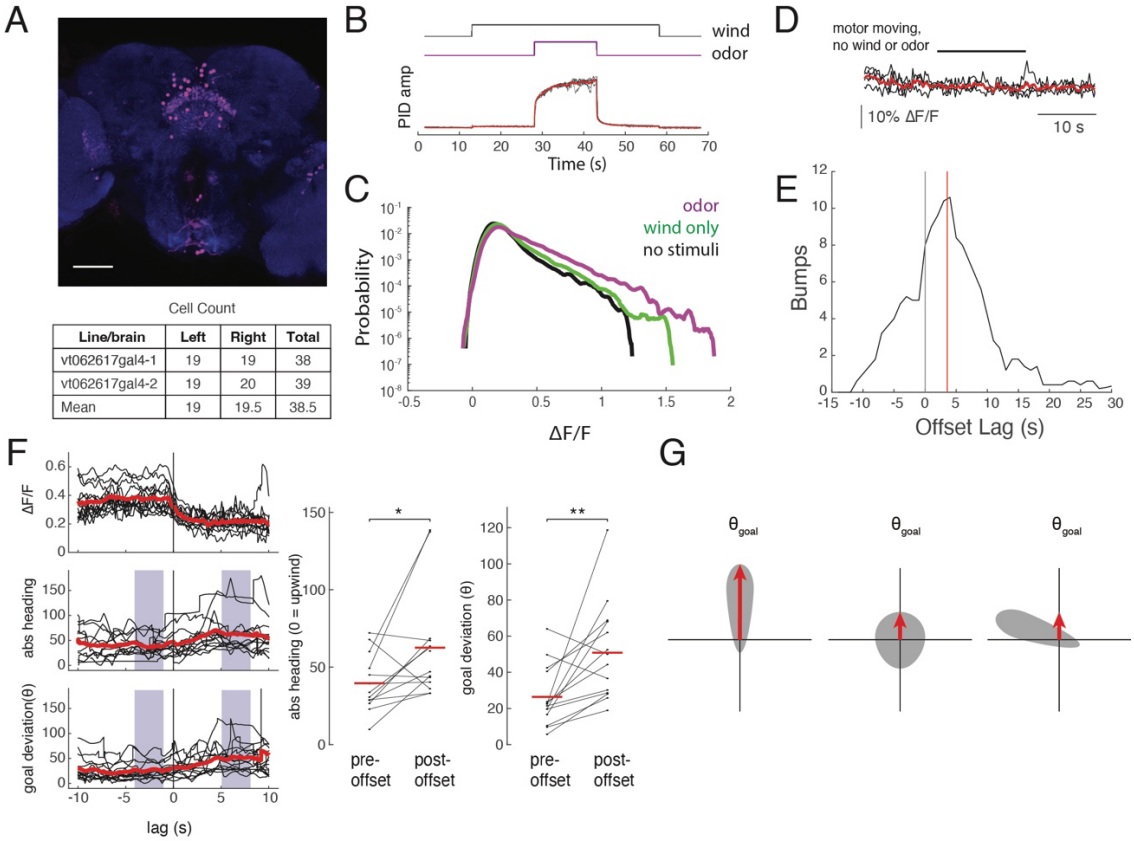

Cell Count

Line/brain	Left	Right	Total
vt062617gal4-1	19	19	38
vt062617gal4-2	19	20	39
Mean	19	19.5	38.5

Supp. Fig. 1: Additional data on VT062617 FB local neuron responses.
A: Top: Confocal image of VT062617>GCaMP brain, stained for GCaMP (pink) and nc82 (blue). Fluorescence signals were imaged from the dorsal (output) projections of FB local neurons. Scale bar is 50μm. Bottom: table of cell body counts for left and right hemispheres in two brains. B: Photoionization detector (PID) recording of odor concentration during typical wind and odor pulse trials (n=6 trials, black: individual trials, red: mean across trials) at the location of the fly. Wind and odor control signals above. C. Distribution of ΔF/F values across all recordings in the presence of odor (purple), during wind only (green) and in the absence of stimuli (black). Total of 328 trials from 15 flies for each condition. D. Average bump amplitude in trials with no wind or odor stimuli, but motor still in closed-loop with heading (n=3-7 trials, N=3 flies). E: Distribution of bump offset times across all flies (n=248 trials from 15 flies) relative to odor OFF (gray line). Mean lag (red line) is 3.64s seconds, well after odor OFF but before wind OFF. F. Deviation from upwind also increases after bump offset but less than deviation from goal direction (paired t-test, abs. heading: p=0.043, goal dev.: p=0.008; N=14). Data on goal deviation reproduced from Fig. 1. Blue boxes indicate measurement windows used in statistical tests. G. Schematic of post-odor goal vector analysis. Projections (red arrows) of heading distribution (blue cloud) onto the direction of travel during the odor period (θ_{goal}) for three scenarios. This metric is high when post-odor heading is has low variability and traveling in the same direction as the odor period (left), and low when headings are either widely distributed (middle) or with low variability but not oriented in the direction of the goal (right).

Figure 2

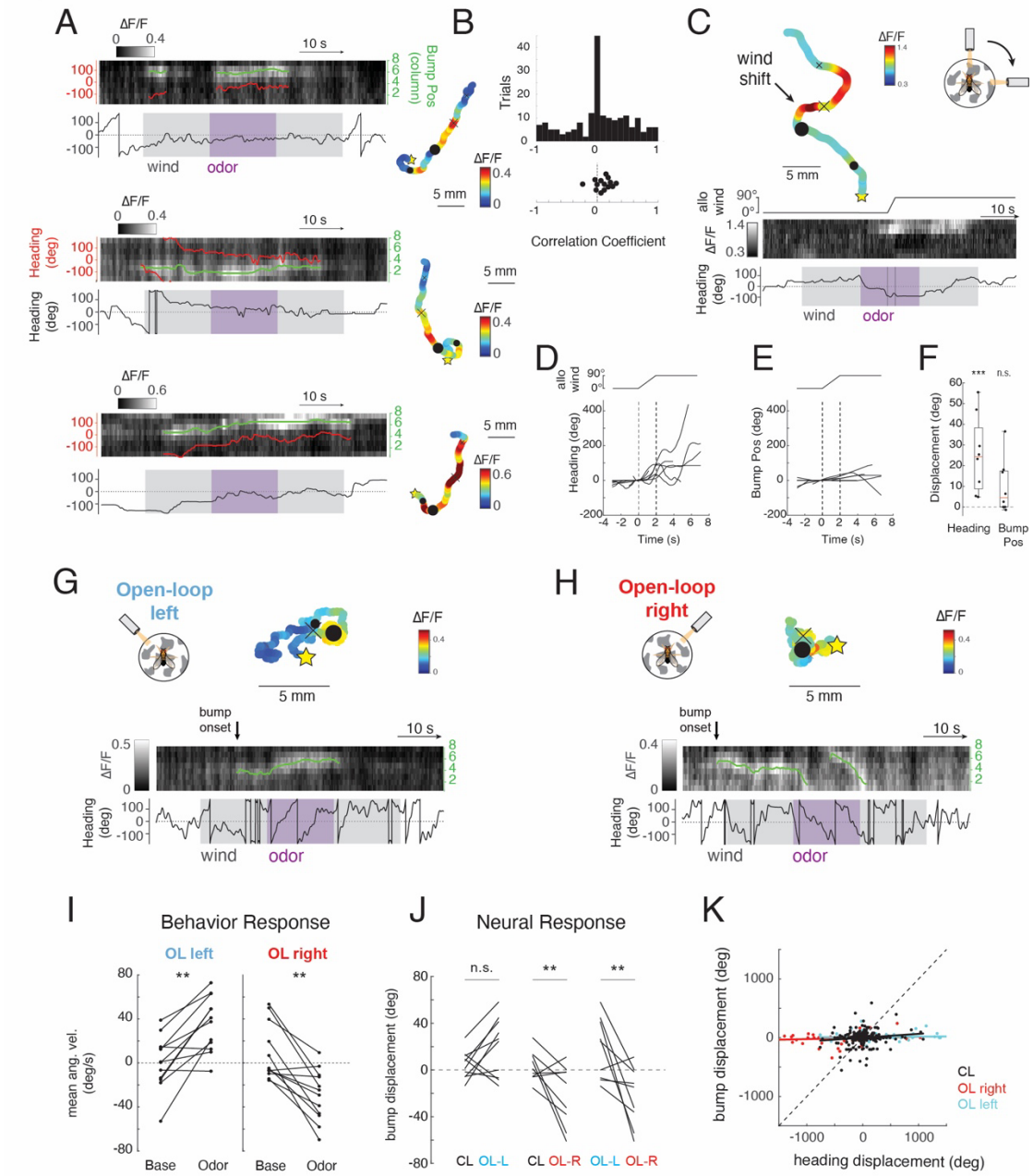

Figure 2: Bump position does not reliably track heading but can slowly shift during persistent turning. A: Three trials demonstrate stability of bump position with variable tracking of heading. Top: two examples where bump position does not change with changes in heading. Bottom: an example where bump position shifts gradually with heading. Heatmaps show activity across columns with bump position (green) and heading (red) overlaid. Heading for whole trial shown below. Right: Trajectories for each trial colored by bump amplitude; symbols as in Fig. 1D. B. Distribution of correlation coefficients between bump position and heading for all trials from all flies (top, n=196 trials) and averaged for each fly (N=14 flies). Pooled data were not significantly different from zero (one-sample t-test, mean=0.043, p=0.22). Fly averages showed a very small positive correlation (mean=0.095, p=0.03). C: Response of a single fly to a 90°

wind shift during odor. Top: fictive 2-D trajectory color-coded by bump amplitude; symbols as in Fig. 1D. Bottom: allocentric wind direction (top), VT062617 activity across columns (middle), and heading (bottom). Note stability of bump position during heading deviation following wind shift. D. Heading response to open-loop wind shift in 8 trials from 4 flies that responded significantly to the wind shift (see Methods). Dashed lines represent start and stop of shift. E. Bump position for the same trials shown in D, offset to an initial position of 0. Note lack of consistent movement. F. Displacement of bump position (left) and heading (right) for the 8 trials shown. Heading displacement is significantly different from zero (mean: 25.41°, one-way t-test: p=0.006) while bump displacement is not (mean: 9.87°; one-way t-test: p=0.072). G: Behavioral and neural responses to open loop wind presented from 45° to the fly's left. Top: fictive 2-D trajectory, color coded by bump amplitude. Middle: VT062617 activity across FB columns with measured bump position (Methods) in green. Bottom: heading. Note repeated turning to the left and associated movement of the bump to the right. H: Same as G for wind presented from 45° to the right. I. Mean angular velocity during odor versus baseline for N=12 flies (2-12 trials per fly). Angular velocity increases when wind is presented from the left (leftward turns, paired t-test p=0.002) and decreases when wind is presented from the right (rightward turns, paired t-test p=0.001). J: Mean bump displacement (in columns) for each fly during closed-loop, open-loop left, and open-loop right trials (N=9 flies with at least 4 trials of each condition, paired t-test, p=0.263, p=0.006, p=0.008). K. Bump displacement vs heading displacement (gain) for all bumps at least 5s duration. Gain is significantly lower than unity (dashed line) for all stimulus types. Black dots: closed-loop trials, red dots: open-loop right trials, cyan dots: open-loop left trials (linear regression slopes=0.065, 0.021, 0.0054, respectively).

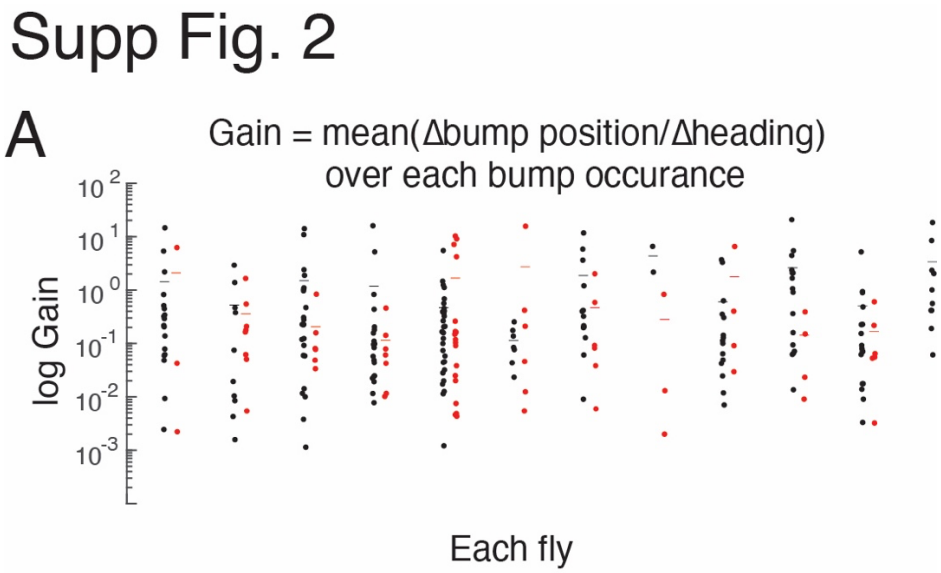

Supp. Fig. 2: Additional data on bump position

A. Distribution of gains (change in bump position vs change in heading) for all bumps for all flies on a log scale. Red: open-loop wind trials, black: closed-loop trials.

Figure 3

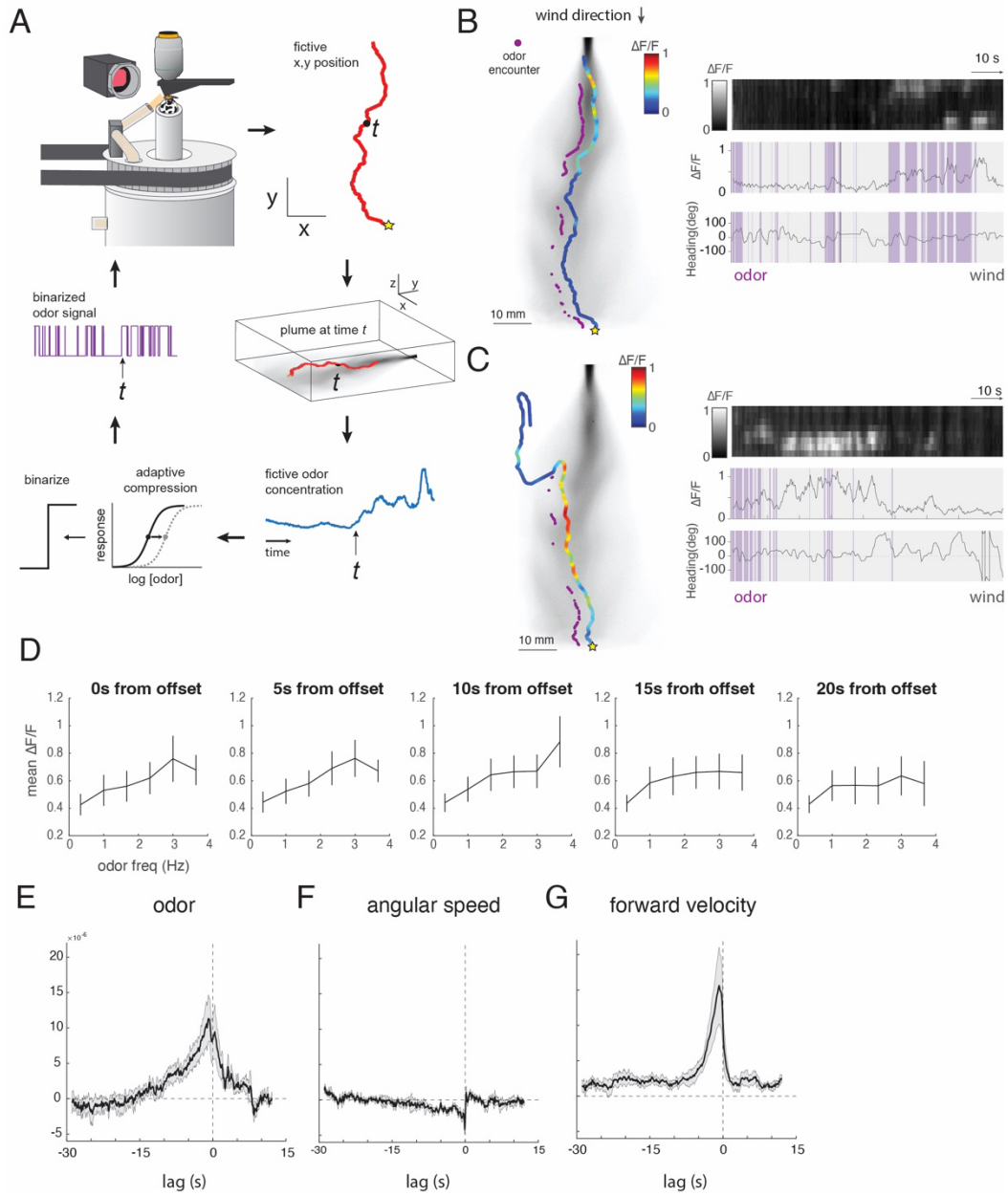

Figure 3: Evidence integration dynamics during closed-loop plume navigation. A: Closed-loop plume navigation paradigm. Time and fictive fly position are used to index into a previously recorded movie of plume dynamics. Measured odor concentrations are converted into binary odor signals based on an adaptive compression algorithm (see Methods). The frequency of the resulting binarized odor signal depends on location and distance from the source. B: Example trial from a fly navigating the virtual plume. Left: virtual 2D trajectory color-coded by bump amplitude, superimposed on a still of the plume movie. Purple dots indicate fictive locations at which odor was presented. Right: activity across FB columns (top), bump amplitude (middle), and heading as a function of time (bottom). Purple bars indicate odor periods. Note minimal responses to early odor presentations and gradual ramping of activity over time. C: Trajectory and activity for another example trial. Note prolonged period of activity associated with straight

walking. D: Mean +/- s.e. of bump amplitude as a function of odor encounter frequency (see Methods) at five times points after the end of the last encounter (t=0,5,10,15,20s after last odor OFF). Data for individual flies shown in Supp Fig. 4B. Only encounters where there was no odor for the duration of the odor OFF period were included (n=1106, 1106, 1097, 1079, 1046 instances from N=6 flies respectively). Bump amplitude increases with odor frequency post-odor periods of up to ~10s. E-G. Linear filters relating neural activity to odor (E), angular speed (F), and forward velocity (G), each mean +/- s.e. for N=6 flies. Odor and forward velocities have an integrating shape with a longer integration time for odor than for forward velocity. Angular speed filter is negative indicating a correlation with decreased angular speed (straight walking).

Supp Fig. 3

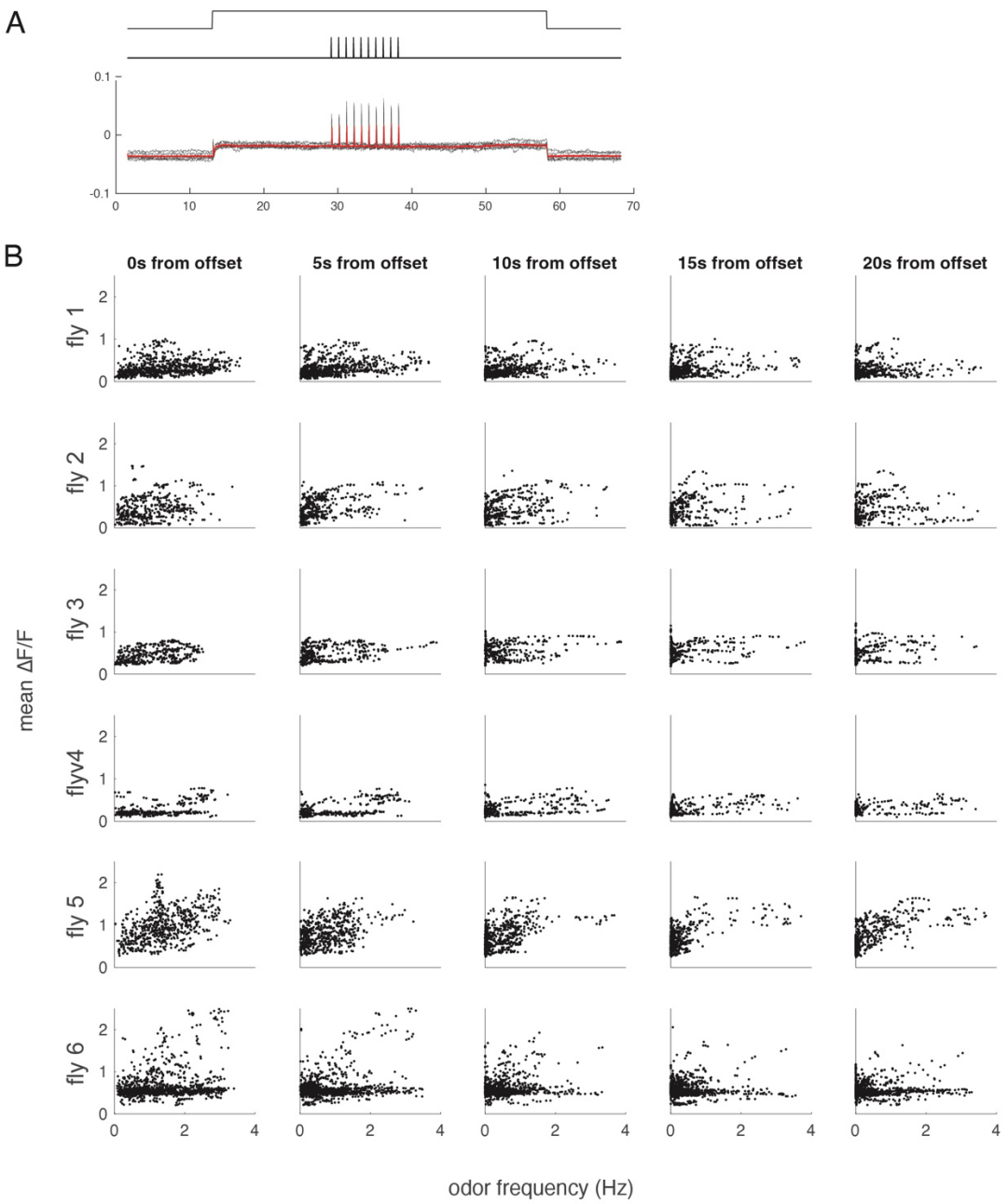

Supp. Fig. 3: Additional data on plume related activity

A. PID measurement of 10ms pulses of odor, the fastest odor pulse possible in virtual odor plume experiments (n=6). Mean trace is in red. B. Bump amplitude as a function of odor encounter frequency and time after odor offset for each individual fly.

Supp Fig. 4

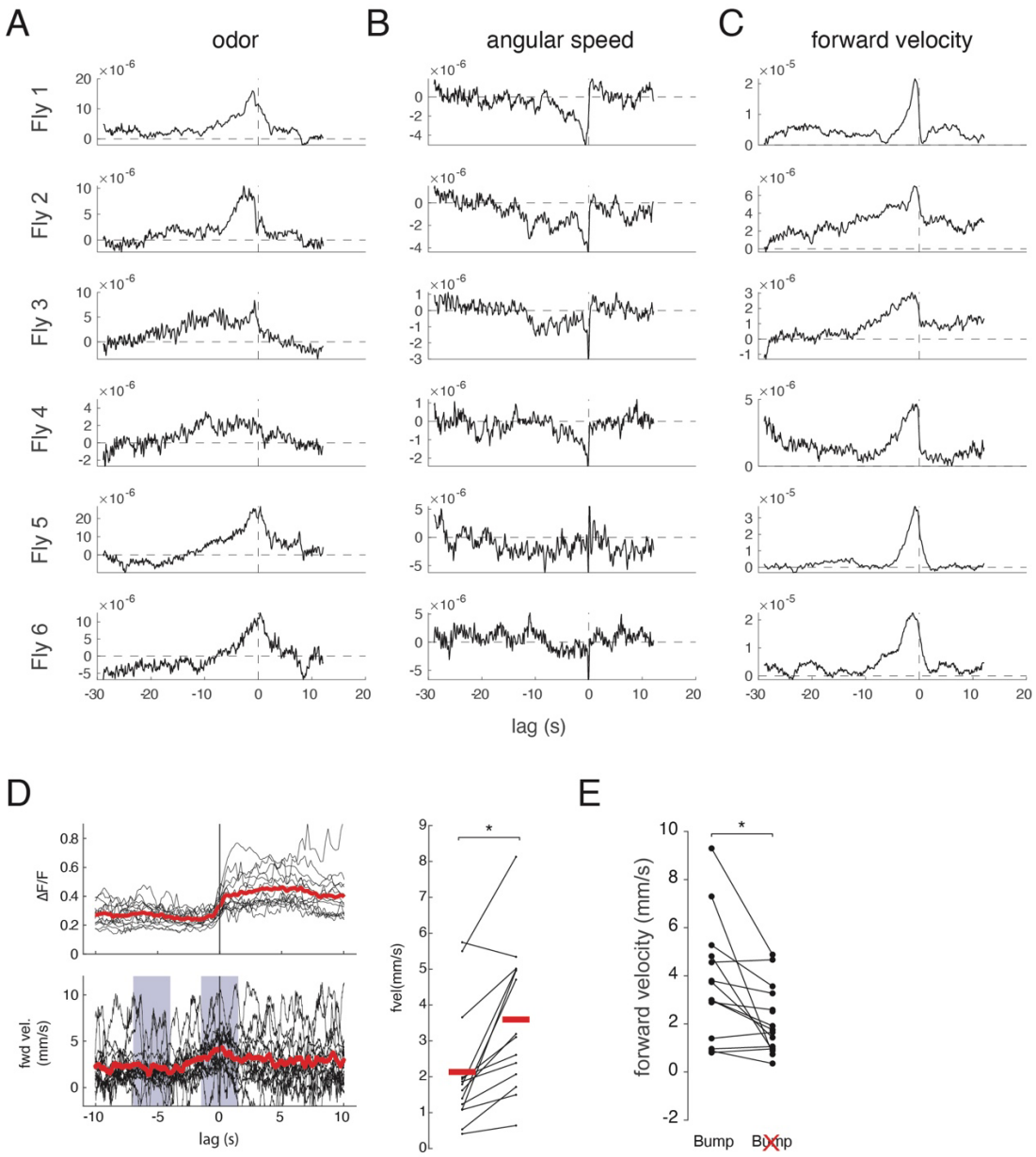

Supp. Fig. 4: Additional data on plume related activity

A-C. Linear filters for odor (A), angular speed (B), and forward velocity (B) for each fly. D. Analysis of locomotor activity relative to bump onset. Left: lower trace shows forward velocity aligned by bump onset (upper), which peaks at bump onset. Red traces represent means across flies (N=14 flies). Right: Mean forward velocity increases during bump onset (pre-onset mean=2.13, post-onset mean=3.60, paired t-test p=0.046, blue boxes indicate analyzed periods.) E. Mean forward velocity during odor is higher in samples with a bump than without (paired t-test, p=0.032, N=14).

Figure 4

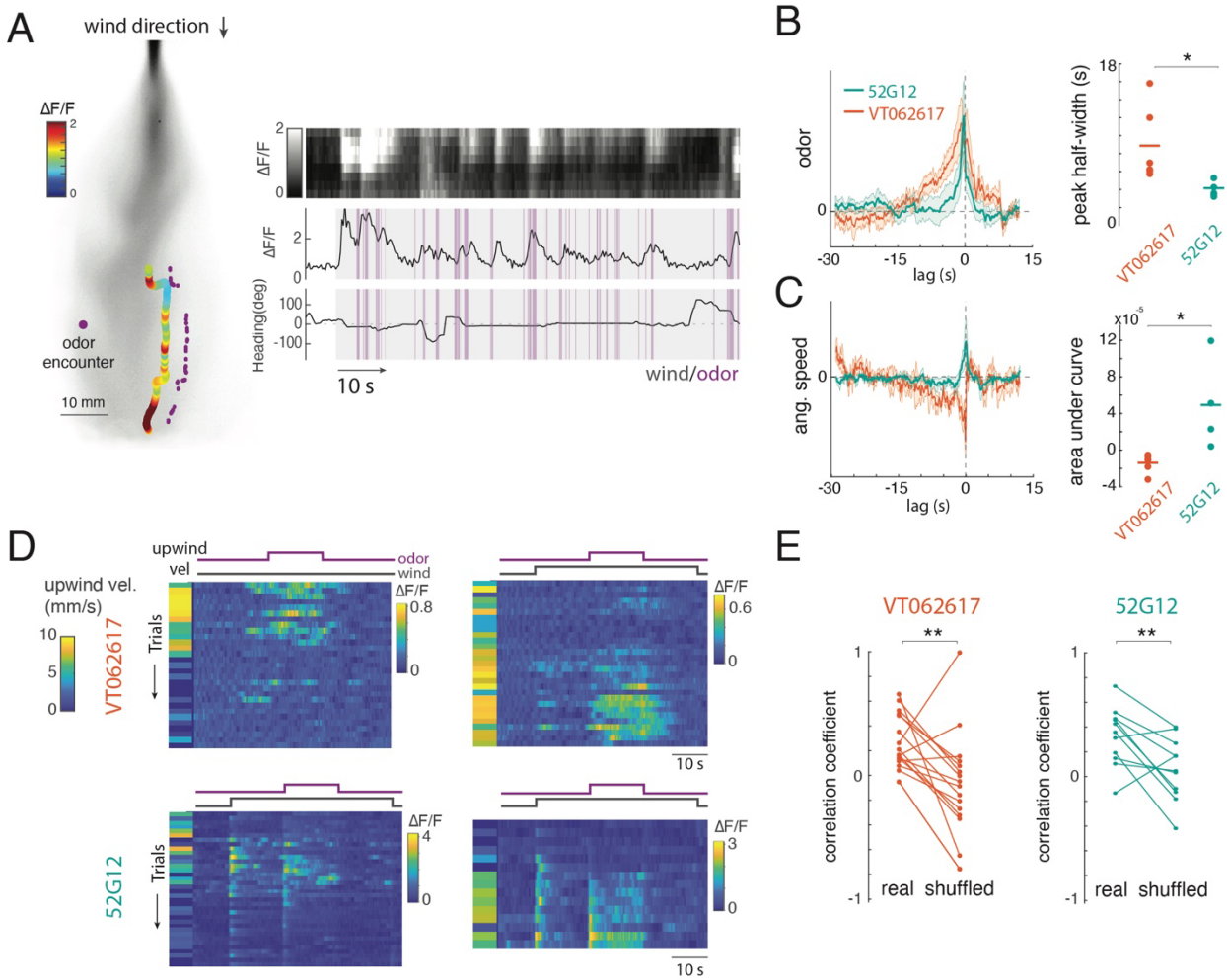

Figure 4: Distinct local dynamics and shared slow dynamics in a population of ventral local neurons. A: Example trial from a fly expressing GCaMP in 52G12 neurons navigating the virtual plume. Left: trajectory color-coded by bump amplitude. Right: activity across FB columns (top), bump amplitude (middle), and heading (bottom) as a function of time. Purple bars indicate odor periods. B: Linear filters relating odor to activity in 52G12 neurons (green, mean +/- S.E. from N=5 flies) and VT062617 neurons (orange, replotted from Fig. 4). 52G12 filters are significantly narrower than VT062617 filters (two-sample t-test, p=0.03). C: Linear filters relating angular speed to activity in 52G12 versus VT062617 neurons. 52G12 filters have a positive area under the curve, indicating a correlation with turning, while VT062617 filters have a negative area (two-sample t-test, p=0.015). D. Example data from 4 flies (top: VT062617, bottom: 52G12) showing upwind velocity during odor (color bar, left) and bump amplitude (right) across trials. I: Correlation coefficients between upwind velocity and total bump amplitude for each fly are significantly higher than for trial-shuffled control data (paired t-test, p-values: VT062617, p=0.001; 52G12, p=0.013).

Supp Fig. 5

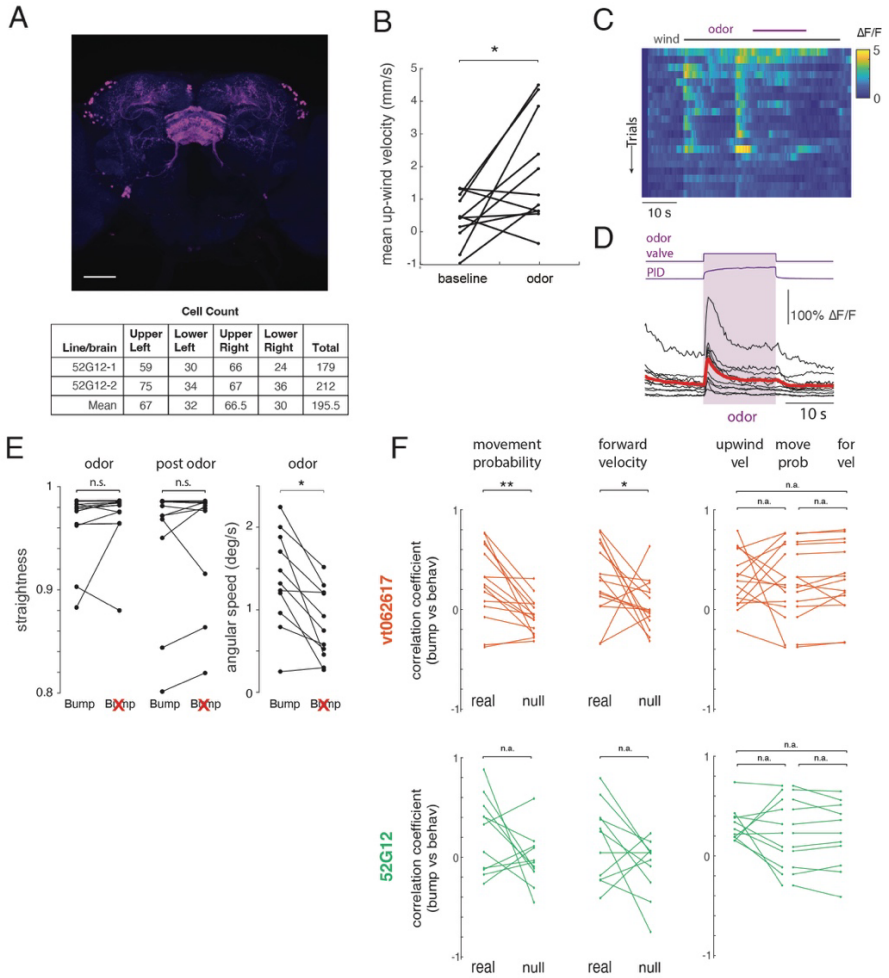

Cell Count

Line/brain	Upper Left	Lower Left	Upper Right	Lower Right	Total
52G12-1	59	30	66	24	179
52G12-2	75	34	67	36	212
Mean	67	32	66.5	30	195.5

Supp. Fig. 5: Additional data on responses of ventral local neurons labeled by 52G12. A: Confocal image of 52G12>GCaMP brains, stained for GCaMP (pink) and nc82 (blue). Scale bar is 50µm. Bottom: table of cell body counts for left/right/upper/lower quadrants of two brains imaged. B: Mean upwind velocities of expressing GCaMP in 52G12 neurons during odor versus baseline (N=11 flies, p=0.018). C: Mean activity in 52G12 neurons over time for all trials for one fly. Note transient responses to wind and odor onset. D: Time course of activity relative to measured odor time course (purple box) for all recorded flies. Black: mean for each fly (n=6 to 30 trials each), red: mean across flies (N=11 flies). E. Left: Mean straightness for 52G12 flies (N=11) in the odor and post-odor periods is not significantly different in the presence versus absence of a bump (paired t-test, during odor p=0.966, post-odor p=0.893). Right: Angular speed during odor is significantly higher in the presence of a bump (paired t-test, p=0.029) F: Correlation coefficients between total bump amplitude and two other behavior metrics—forward velocity and movement probability— for each fly of the two genotypes. In VT062617 flies, correlation coefficients are significantly higher than for trial-shuffled control data (N=15, paired t-tests: pmove p=0.004, fwd. vel. p= 0.04). For 52G12 flies, correlation coefficients are not significantly different from shuffled data (N=11, paired t-test: pmove p=0.11, fwd. vel. p=0.084), In neither line were fly means of each metric significantly different from each other (right; paired t-test, all comparisons p>0.05).

Figure 5

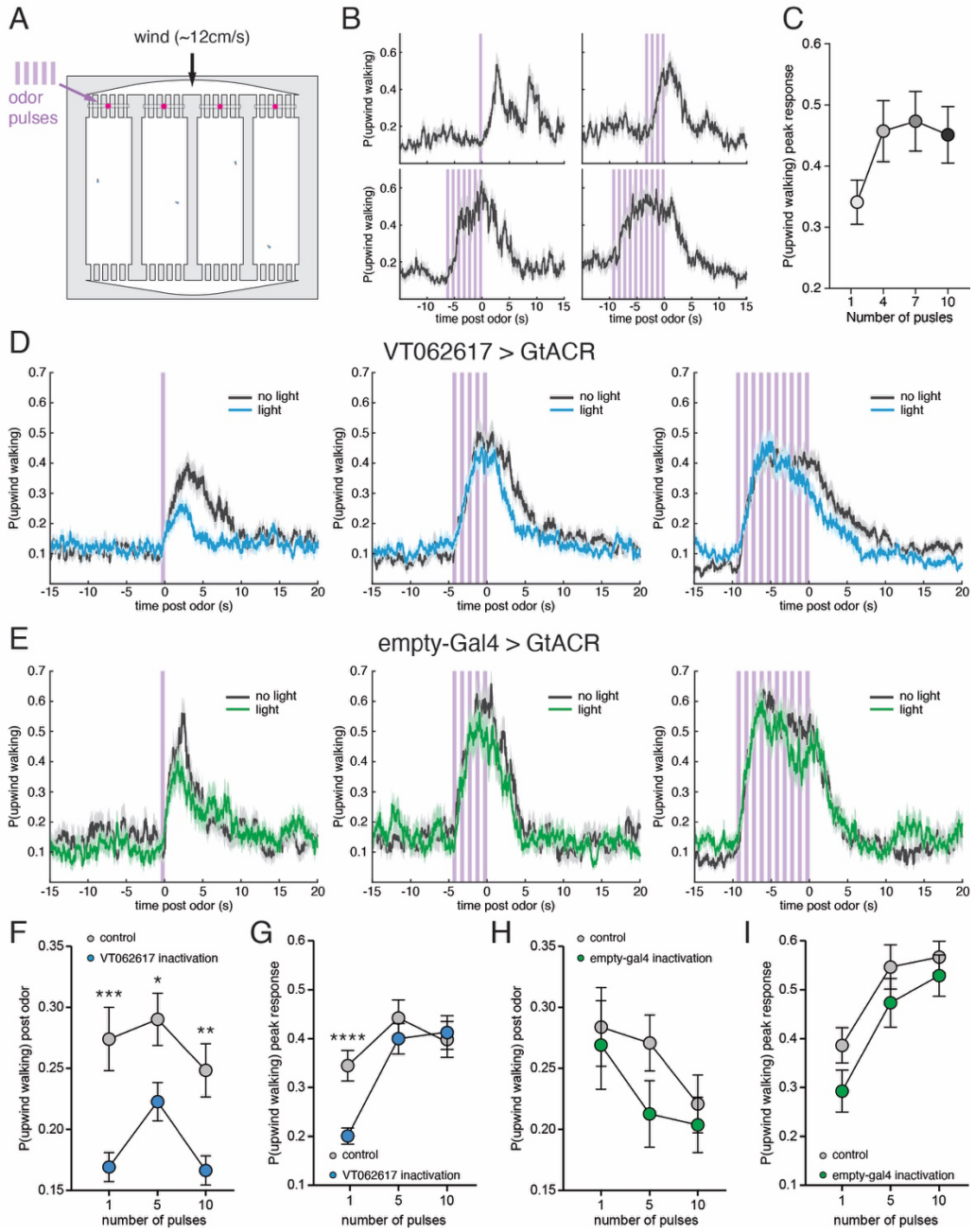

Figure 5. VT062617 neurons are causally required for persistent upwind navigation. A: Schematic of top view of behavioral apparatus used to track freely moving flies, showing odor and wind inputs. B: Probability of upwind walking as a function of time, for different numbers of odor pulses (500 ms each) in wild type flies (1 pulse: 246 trials from N=30 flies; 4 pulses: n=226 trials from N=28 flies; 7 pulses: 213 trials from N=29 flies; 10 pulses: 246 trials from N=30 flies). C: Mean probability of upwind walking during peak response period (2-6 s, relative to odor start) for each pulse number. Data are mean +/- SEM across flies. D: Probability of upwind walking in VT062617>GtACR flies responding to 1, 5, or 10 pulses of odor with light OFF (black, 1 pulse:

n=381 trials from N=30 flies; 5 pulses: n=418 trials from N=30 flies; 10 pulses: n=463 trials from N=30 flies) or light ON (blue, 1 pulse: n=405 trials from N=30 flies; 5 pulses: n=422 trials from N=30 flies; 10 pulses: n=450 trials from N=30 flies). Note decrease in upwind walking probability after odor OFF on light ON trials across stimuli. E: Probability of upwind walking in empty-gal4>GtACR flies responding to the same stimuli with light OFF (black, 1 pulse: n=261 trials from N=26 flies; 5 pulses: n=246 trials from N=26 flies; 10 pulses: n=318 trials from N=28 flies) and light ON (blue, 1 pulse: n=294 trials from N=26 flies; 5 pulses: n=310 trials from N=28 flies; 10 pulses: n=292 trials from N=27 flies). F: Mean probability of upwind walking during the 10 s post-odor in VT062617 > GtACR1 during light ON (blue) is significantly lower than in light OFF (grey) trials (Bonferroni-corrected (α=0.0167) ranksum test: 1 pulse (*N*=30): *p*=0.0002, 5 pulses (*N*=30): *p*=0.0128, 10 pulses (*N*=30): *p*=0.0010). G: Mean probability of upwind walking during peak response period (2-6 s, relative to odor start) for VT062617 > GtACR1 flies with light ON (blue) and light OFF (grey, Bonferroni-corrected (α=0.0167) ranksum test: 1 pulse (*N*=30): *p*<0.0001, 5 pulses (*N*=30): *p*=0.2367, 10 pulses (*N*=30): *p*=0.7151). H: Same comparison as F, but for empty-gal4 > GtACR1 flies during light ON (green) and light OFF (grey) trials: 1 pulse (*N*=25): *p*=0.4742, 5 pulses (*N*=27): *p*=0.0463, 10 pulses (*N*=28): *p*=0.3989. I: Same comparison as G, but for empty-gal4 > GtACR1 flies during light ON (green) and light OFF (grey) trials: 1 pulse (*N*=25): *p*=0.0367, 5 pulses (*N*=28): *p*=0.0187, 10 pulses (*N*=28): *p*=0.4846.

Supp. Figure 6

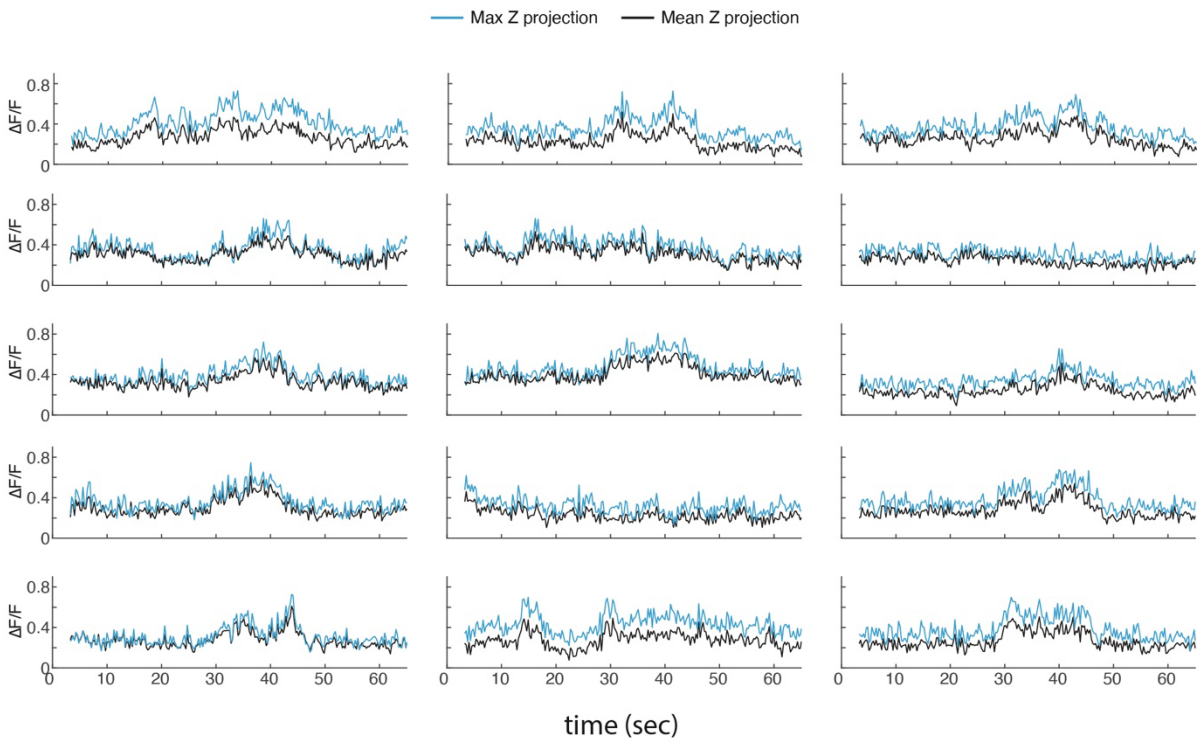

Supp. Fig. 6. ∆F/F calculated from either max or mean projections across z planes are highly correlated

Example trials of bump amplitude calculated using the max (cyan) vs mean (black) across z-planes of the volume. Both signals are highly correlated, with the max projection with slightly higher signal to noise, hence the max projection was used for all ∆F/F values .